Available online at www.sciencedirect.com
SCIENCE DIRECT®
Journal of Computational Physics 192 (2003) 422–451
JOURNAL OF COMPUTATIONAL PHYSICS
www.elsevier.com/locate/jcp

Mathematical balancing of flux gradient and source terms prior to using Roe's approximate Riemann solver

Benedict D. Rogers, Alistair G.L. Borthwick *, Paul H. Taylor

Department of Engineering Science, University of Oxford, Parks Road, Oxford OX1 3PJ, UK

Received 28 August 2002; received in revised form 15 July 2003; accepted 15 July 2003

Abstract

An algebraic technique is presented for balancing flux gradients and source terms when applying Roe's approximate Riemann solver in finite volume schemes. The numerical imbalance is eradicated by reformulating the governing matrix hyperbolic system of conservation laws in terms of deviations away from an unforced but separately specified equilibrium state. Thus, balancing is achieved by the incorporation of this extra physical information and bypasses conventional numerical treatments of the imbalance. The technique is first applied to the shallow water equations. Simulations of benchmark flows including wind-induced flow in a two-dimensional basin, transcritical flow in a one-dimensional channel and wave propagation over a two-dimensional hump are in close agreement with analytical solutions and predictions by alternative numerical schemes. The technique is then applied to a more complicated coupled pair of equation sets, the hyperbolic period- and depth-averaged ray-type wave conservation and modified shallow water equations that describe wave current interaction in the nearshore zone at the coast. Reasonable agreement is obtained with laboratory measurements of wave diffraction behind a submerged elliptical shoal [Coastal Engrg. 6 (1982) 255] and of wave-induced nearshore currents at a half-sinusoidal beach [Wave-induced nearshore currents, Ph.D. Thesis, Liverpool University, UK, 1981].

Keywords: Roe's approximate Riemann solver; Flux gradients; Source terms; Shallow-water equations; Wave-conservation equations

1. Introduction

Prediction of flows with discontinuities, such as aerodynamic shock waves or hydraulic jumps, has been a great challenge to numerical schemes for both gas dynamics and hydrodynamics. In a landmark paper, Godunov [17] presented a treatment of discontinuities in hyperbolic systems by assuming piecewise constant distributions of data within computational grid cells and solving the resultant discontinuities or Riemann problems that exist at each cell interface. By upwinding the flux within an integral conservation form of the governing equations, Godunov-type methods account for the physically correct propagation of

* Corresponding author. Tel.: +44-1865-273047; fax: +44-1865-273010.
E-mail address: alistair.borthwick@eng.ox.ac.uk (A.G.L. Borthwick).

0021-9991/$ - see front matter © 2003 Elsevier B.V. All rights reserved.
doi:10.1016/j.jcp.2003.07.020

information throughout the flow field by solving sets of Riemann problems over the entire computational domain. Many approximate Riemann solvers now exist to evaluate numerically convective fluxes. One of the most popular is the method due to Roe [30,31] which has been widely researched, particularly for steady aerodynamic flows.

The advantages of using Riemann solvers to describe rapidly varying shallow water flows became apparent in the early 1990s. The shallow-water equations (SWEs) describe the conservation of mass and momentum in shallow water bodies, and are particularly amenable to solution by finite volume Godunov-type approaches where Roe's approximate Riemann solver can be used to evaluate inviscid fluxes [1,3,14].

Although Roe's approximate method is robust, difficulties arise in solving the Riemann problem when source terms are included in the analysis (for details see [16]). Essentially, a numerical imbalance is created by the artificial splitting of physically meaningful terms in the governing equations between flux gradients and source terms in order to generate a mathematically hyperbolic formulation. These terms are then evaluated by different methods at different locations within the computational grid creating the numerical imbalance.

The imbalance problem is particularly acute for the SWEs where the surface gradient term within the momentum equations is conventionally split into an artificial flux gradient and a source term that includes the effect of the bed slope. Thus, many numerical solvers of the SWEs based on the conventional formulation give unphysical results for flows over physically realistic variable bathymetries, solely because of this mathematically convenient splitting. Nugic [28] observed that very poor results were obtained for cases of shallow water flow with variable depth, referring to the problem as numerical incompatibility. Nugic proposed a revised mathematical formulation of the SWEs, by reallocating all bed-slope related flux gradients to the source terms. Ambrosi [2] noted that the effectiveness of using Roe's approximate Riemann solver was lost when the bottom slope varied, giving a quantitative estimation of the error of the scheme as first-order, but accepted that the quiescent still water solution was not computed, in favour of preserving the formal accuracy of the scheme.

Recently, Vázquez-Cendón [38] used numerical upwinding of the source terms to achieve equilibrium between flux gradient and source terms in the shallow water equations. Hubbard and García-Navarro [22] and García-Navarro and Vázquez-Cendón [15] have since extended this numerical treatment to higher-order total variation diminishing (TVD) schemes. Meanwhile, Zhou et al. [41] suggested an alternative piecewise linear reconstruction of the surface gradient term in the SWEs, which was demonstrated using an HLL Riemann solver. LeVeque [24] proposed a wave propagation algorithm by artificially introducing another discontinuity within each computational cell to account for the propagation of source terms. Although suitable for quasi-steady conditions, LeVeque's method is reportedly less robust when predicting steady transcritical flows that contain shocks. In an investigation of different explicit schemes, Burguete and García-Navarro [9] presented conservative schemes in a non-conservative formulation of the equations with flux-adjusted source terms discretised using either a semi-implicit or upwinding technique. Gascón and Coberán [16] present another approach to deal with the balancing difficulty by transforming non-homogeneous conservation laws into homogeneous ones by introducing a new flux generated by the addition to the physical flux of the primitive of the source term.

Most of the foregoing approaches attempted to rectify the problematic conventional formulation of the SWEs using a numerical treatment. However, by mathematically rearranging the SWEs to be balanced prior to their numerical solution by including quiescent still-water (or equilibrium) conditions, Rogers et al. [33] avoided the computational effort incurred by the numerical balancing approaches such as upwinding of source terms. Importantly, however, many conservation equations are not as simple as the SWEs, making most balancing methods difficult to apply to formulations that include complicated combinations of derivatives. Hence, the algebraic approach of Rogers et al. [33] to the flux-gradient source-term problem provides the motivation for the present work.

Section 2 of the present paper describes the difficulty encountered when balancing the flux gradient and source terms for an example case of the one-dimensional shallow water equations. Section 3 develops a generalisation of the technique presented by Rogers et al. [33] for mathematically balancing the shallow water equations. In Section 4, it is confirmed that the balanced SWEs solver derived by Rogers et al. is a particular case of the generalised method and results are presented that demonstrate the validity of the approach. In Section 5, the applicability of the new technique is further illustrated by mathematically conditioning a more complex set of equations that describe period-averaged wave–current interaction in the nearshore zone which cannot be straightforwardly rewritten in a convenient mathematical form.

2. The nature of the problem

The SWEs are derived by depth-averaging the Reynolds equations and express conservation of mass and momentum. It is assumed that vertical motions are negligible and that pressure is hydrostatic. In conservation form, the two-dimensional shallow water equations are:

$$\frac{\partial h}{\partial t}+\frac{\partial(uh)}{\partial x}+\frac{\partial(vh)}{\partial y}=0, \tag{2.1a}$$

$$\frac{\partial(uh)}{\partial t}+\frac{\partial(u^2h)}{\partial x}+\frac{\partial(uvh)}{\partial y}-\varepsilon\left(\frac{\partial(hu_x)}{\partial x}+\frac{\partial(hu_y)}{\partial y}\right)=\frac{\tau_{wx}-\tau_{bx}}{\rho}-gh\frac{\partial\zeta}{\partial x}+hfv, \tag{2.1b}$$

$$\frac{\partial(vh)}{\partial t}+\frac{\partial(uvh)}{\partial x}+\frac{\partial(v^2h)}{\partial y}-\varepsilon\left(\frac{\partial(hv_x)}{\partial x}+\frac{\partial(hv_y)}{\partial y}\right)=\frac{\tau_{wy}-\tau_{by}}{\rho}-gh\frac{\partial\zeta}{\partial y}-hfu, \tag{2.1c}$$

where ζ is the free surface elevation above the still water level h_s, h $(=\zeta+h_s)$ is the total water depth, u and v are the depth-averaged velocities in the x- and y-directions, respectively, t is the time, u_x, u_y and v_x, v_y are spatial derivatives of the velocity components, g is the gravitational acceleration, ρ is the water density, τ_{wx} and τ_{wy} are surface stresses, τ_{bx} and τ_{by} are bed friction stresses, ϵ is the kinematic eddy viscosity coefficient and f is the Coriolis parameter.

When formulating a Riemann solver for the SWEs it is necessary to rewrite Eqs. (2.1a)–(2.1c) as a system of hyperbolic equations. To achieve this, it is conventional to split the $gh\partial\zeta/\partial x$ term between flux gradients and source terms (e.g., [40]) to give:

$$gh\frac{\partial\zeta}{\partial x}=\frac{\partial}{\partial x}\left(\frac{1}{2}gh^2\right)+ghS_{ox}\quad\text{(surface gradient term}\rightarrow\text{flux gradient}+\text{source term)}, \tag{2.2}$$

where S_{ox} is the bed slope in the x-direction. A similar treatment is applied in the y-direction. Of the Roe-type Riemann solvers for the SWEs that use this approach, many have been validated using test cases with either a flat bottom or a uniform slope (e.g. [1,3,40], etc.). However, numerical difficulties arise with the splitting (2.2) when considering non-uniform bathymetries. If we consider the inviscid one-dimensional shallow water equations in the x-direction only, Eqs. (2.1a)–(2.1c) become

$$\frac{\partial h}{\partial t}+\frac{\partial(uh)}{\partial x}=0, \tag{2.3a}$$

$$\frac{\partial(uh)}{\partial t}+\frac{\partial(u^2h+\frac{1}{2}gh^2)}{\partial x}=\frac{\tau_{wx}-\tau_{bx}}{\rho}-ghS_{ox}, \tag{2.3b}$$

where the surface gradient term splitting of Eq. (2.2) has been incorporated as an extra artificial flux term and a source term containing the bed slope S_{ox}.

Within a finite volume scheme, the one-dimensional SWEs can be written in integral form as

$$\frac{\partial}{\partial t}\int_{\Omega}\mathbf{q}\,\mathrm{d}\Omega+\int_{\Omega}\frac{\partial\mathbf{f}}{\partial x}\,\mathrm{d}\Omega=\int_{\Omega}\mathbf{h}\,\mathrm{d}\Omega, \tag{2.4}$$

where Ω is the problem domain, t is the time, x is a continuous real variable, $\mathbf{q}$ is the vector of conserved variables, $\mathbf{f}$ is a flux vector and $\mathbf{h}$ is the vector of source terms. The vectors $\mathbf{q}$, $\mathbf{f}$ and $\mathbf{h}$ are given by

$$\mathbf{q}=\begin{bmatrix}h\\ uh\end{bmatrix},\quad \mathbf{f}=\begin{bmatrix}uh\\ u^2h+\frac{1}{2}gh^2\end{bmatrix}\quad\text{and}\quad \mathbf{h}=\begin{bmatrix}0\\ (\tau_{wx}-\tau_{bx})/\rho-ghS_{ox}\end{bmatrix}. \tag{2.5}$$

By applying Gauss' theorem to the second term in Eq. (2.4),

$$\frac{\partial}{\partial t}\int_{\Omega}\mathbf{q}\,\mathrm{d}\Omega+\oint_{S}\mathbf{f}\,\mathrm{d}S=\int_{\Omega}\mathbf{h}\,\mathrm{d}\Omega, \tag{2.6}$$

which for each cell can be more conveniently rewritten as

$$\left.\frac{\partial V\mathbf{q}}{\partial t}\right|_{i}=-\oint_{\partial C_i}\mathbf{f}_i\,\mathrm{d}S+V_i\mathbf{h}_i=-(\mathbf{f}_{\mathrm{E}}-\mathbf{f}_{\mathrm{W}})\Delta s+V_i\mathbf{h}_i, \tag{2.7}$$

where $\mathbf{q}_i$ and $\mathbf{h}_i$ are the cell centre values, V_i denotes the area of cell, ∂C_i is the path of integration, which is along all cell edges (the flux out of each face being assumed uniform), $\mathbf{f}_{\mathrm{E}}$ and $\mathbf{f}_{\mathrm{W}}$ are the vector fluxes through the east and west faces of each cell respectively and Δs is the length of each cell.

By adopting Roe's approximate Riemann solver at each cell edge, the inviscid fluxes can be evaluated as follows:

$$\mathbf{f}_{i,j}=\frac{1}{2}\left[\mathbf{f}\left(\mathbf{q}^{+}_{i,j}\right)+\mathbf{f}\left(\mathbf{q}^{-}_{i,j}\right)-|\mathbf{A}|\left(\mathbf{q}^{+}_{i,j}-\mathbf{q}^{-}_{i,j}\right)\right], \tag{2.8}$$

where $|\mathbf{A}|=\mathbf{R}|\mathbf{\Lambda}|\mathbf{L}$, $\mathbf{q}^{+}_{i,j}$ and $\mathbf{q}^{-}_{i,j}$ are reconstructed right and left Riemann states, respectively, at the cell interface located between adjacent cells i and j, $\mathbf{A}$ is the flux Jacobian evaluated using $\mathbf{R}$ and $\mathbf{L}$, the right and left eigenvector matrices of $\mathbf{A}$, respectively, and $|\mathbf{\Lambda}|$ is a diagonal matrix of the absolute values of the eigenvalues of $\mathbf{A}$.

To demonstrate the root cause of the numerical incompatibility, consider the one-dimensional situation in Fig. 1(a) that depicts water initially at rest in a discretised basin with a varying bed slope. The bottom is assumed to be smooth so there is no bed friction. Importantly, there are also no wind or surface shear stresses, so there is no input driving force into the system that could cause movement of water. Therefore, the water should remain perfectly still.

Initially, when the water is at rest, the matrix $|\mathbf{A}|$ is given by

$$|\mathbf{A}|=\begin{bmatrix}|c| & 0\\ 0 & |c|\end{bmatrix}. \tag{2.9}$$

However, across the interface between cell i and cell j, one can see that $h^{+}\neq h^{-}$, so that in Eq. (2.8), an unphysical non-zero flux is generated in the initially still water:

$$\mathbf{f}_{i,j}=\begin{bmatrix}-\frac{1}{2}|c|(h^{+}-h^{-})\\ \frac{1}{2}\left\{\frac{1}{2}g(h^{+})^2-\frac{1}{2}g(h^{-})^2\right\}\end{bmatrix}, \tag{2.10}$$

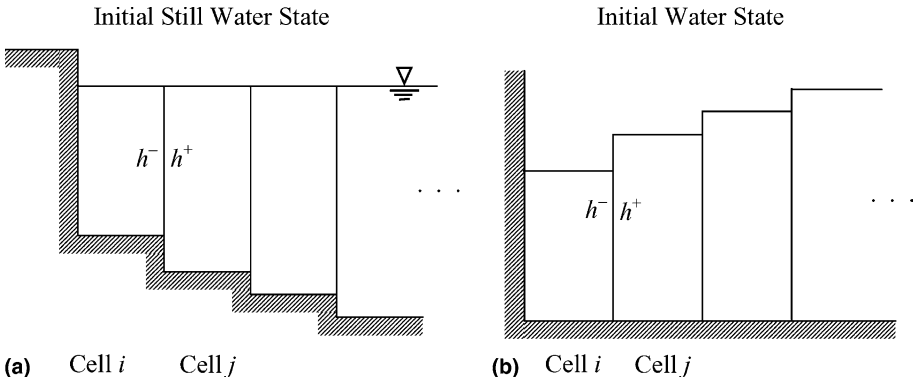

Fig. 1. (a) Initial still water state creating unphysical fluxes. (b) Indistinguishable initial water state creating the same physical fluxes.

which along with another flux at the wall on the other side of the cell i is clearly not balanced by an unphysical driving input into the system generated in the source term by

$$\mathbf{h} = \begin{bmatrix} 0 \\ -gh_i S_{ox} \end{bmatrix}. \tag{2.11}$$

Once this numerical imbalance is integrated in time, the next time step of the simulation creates other unphysical fluxes based on this one and so on. The end result is that the model cannot even simulate still water. Essentially, on the very first time step, the model cannot tell the difference between the fluxes induced by the two different cases depicted in Fig. 1. The crucial difference between the situations depicted in Fig. 1 is that in 1(b), the bed slope is flat so the problem of source-term flux-gradient balancing is eradicated. The problem still exists even if higher-order variable reconstruction schemes are used.

Consider the case of a circular lake of non-uniform bathymetry given by $h = (0.5 + \sqrt{(0.5 - 0.5r/R_o)})/1.3$, where r is the radial distance from the centre of the basin and $R_o = 192$ m is its boundary radius (see Fig. 2(a)). In this case, the full two-dimensional shallow water equations are applicable. Initial conditions are water at rest with a horizontal free surface. The plan domain is discretised spatially onto a quadtree grid of interior level 6 and perimeter level 8 (see [33] for an explanation of the quadtree grid system). The shallow water solver is integrated forward in time using time steps of $\Delta t = 0.05$ s, in the absence of bed friction, turbulent eddy viscosity and Coriolis force. Fig. 2(b) shows the depth-averaged velocity vectors at $t = 1$ s, where it is evident that the water is in motion even though there is no input driving force. The situation is worst at the basin perimeter where the bed slope undergoes the greatest change and numerical incompatibility is worst.

Rogers et al. [33] proposed balancing the flux gradients and source terms by a mathematical manipulation of the troublesome bed-slope term, namely

$$gh\frac{\partial \zeta}{\partial x} = \frac{\partial}{\partial x}\left(\frac{1}{2}g(\zeta^2 + 2\zeta h_s)\right) + g\zeta S_{ox}. \tag{2.12}$$

Within the finite volume Godunov-type scheme, this approach has the advantage that the flow is driven only by deviations of the free surface elevation from the still water level. Application of this mathematical conditioning of the shallow water equations entirely eradicates the numerical imbalance in Roe's approximate solver, and so the water remains quiescent throughout the domain at all times during the

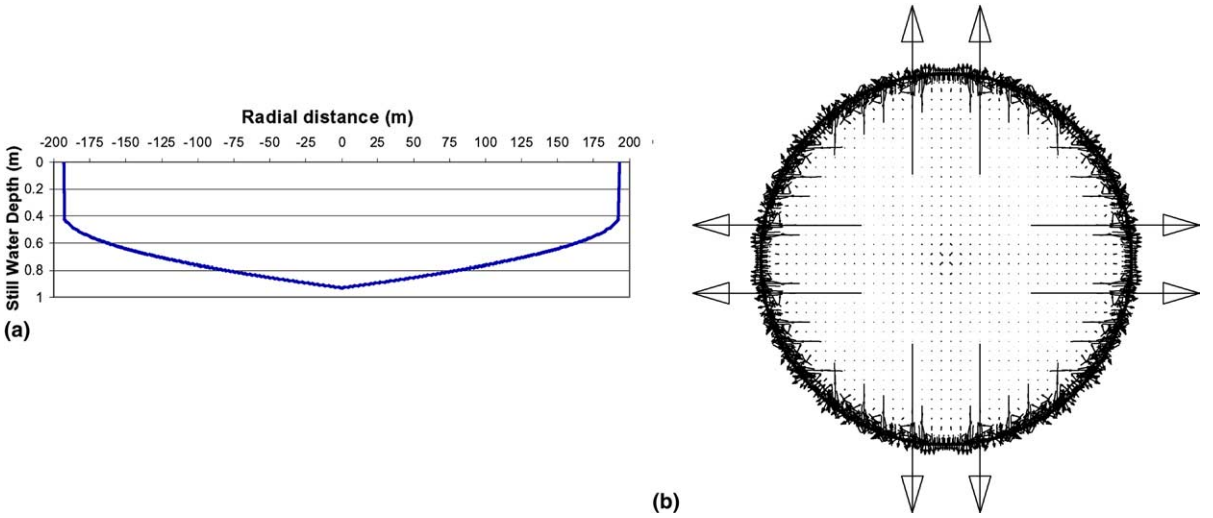

Fig. 2. (a) Circular basin bathymetry – cross-section. (b) Velocity vectors for unbalanced still water case.

simulation. The balanced simulation of wind-induced circulation in the circular basin will be examined later in Section 4.2.

3. Derivation of a new flux gradient and source term balancing technique

Source and flux gradient terms in the discretised governing equations are split but rarely balanced when using Roe's approximate Riemann solver. This splitting has traditionally been done to ensure hyperbolicity but without regard to a proper numerical balance, leading to spurious numerical errors and unphysical solutions. Rogers et al. [33] split the troublesome terms in an algebraic manner that ensures mass and momentum conservation. A generalisation of the technique presented by Rogers et al. now follows.

3.1. Reformulation

Consider a system of one-dimensional hyperbolic conservation laws integrated over a finite volume, Ω,

$$\frac{\partial}{\partial t}\int_{\Omega}\mathbf{q}\,\mathrm{d}\Omega+\int_{\Omega}\frac{\partial\mathbf{f}(\mathbf{q})}{\partial x}\,\mathrm{d}\Omega=\int_{\Omega}\mathbf{h}\,\mathrm{d}\Omega. \tag{3.1}$$

Applying Gauss's theorem to the second term allows Eq. (3.1) to be solved conventionally using any of the standard finite volume methods. However, in order to balance flux gradient and source terms, we now add and subtract equilibrium (or quiescent) values of the integrated flux gradients to Eq. (3.1) to give

$$\frac{\partial}{\partial t}\int_{\Omega}\mathbf{q}\,\mathrm{d}\Omega+\int_{\Omega}\left(\frac{\partial\mathbf{f}(\mathbf{q})}{\partial x}-\frac{\partial\mathbf{f}(\mathbf{q}^{\mathrm{eq}})}{\partial x}\right)\mathrm{d}\Omega=\int_{\Omega}\mathbf{h}\,\mathrm{d}\Omega-\int_{\Omega}\frac{\partial\mathbf{f}(\mathbf{q}^{\mathrm{eq}})}{\partial x}\,\mathrm{d}\Omega, \tag{3.2}$$

where the superscript eq denotes equilibrium values. The use of the superscript eq is deliberately general so that, depending on the situation being modelled, eq could refer to still water conditions or equilibrium conditions to allow one to drive a simulation to steady state. Eq. (3.2) can be written as

$$\frac{\partial}{\partial t}\int_{\Omega}\mathbf{q}\,\mathrm{d}\Omega+\int_{\Omega}\frac{\partial}{\partial x}[\mathbf{f}(\mathbf{q})-\mathbf{f}(\mathbf{q}^{\mathrm{eq}})]\,\mathrm{d}\Omega=\int_{\Omega}\mathbf{h}^{*}\,\mathrm{d}\Omega, \tag{3.3}$$

where the equilibrium-corrected source term $\mathbf{h}^{*}$ is given by

$$\mathbf{h}^{*}=\mathbf{h}-\frac{\partial\mathbf{f}(\mathbf{q}^{\mathrm{eq}})}{\partial x}. \tag{3.4}$$

Also, the vector of conserved variables $\mathbf{q}$ is given by

$$\mathbf{q}=\mathbf{q}^{\mathrm{eq}}+\mathbf{q}', \tag{3.5}$$

where $\mathbf{q}'$ is the deviation of $\mathbf{q}$ from the equilibrium or still water value such that $\partial\mathbf{q}^{\mathrm{eq}}/\partial t=0$. Eq. (3.3) therefore becomes

$$\frac{\partial}{\partial t}\int_{\Omega}\mathbf{q}'\,\mathrm{d}\Omega+\int_{\Omega}\frac{\partial\mathbf{f}'}{\partial x}\,\mathrm{d}\Omega=\int_{\Omega}\mathbf{h}^{*}\,\mathrm{d}\Omega, \tag{3.6}$$

where $\mathbf{f}'=\mathbf{f}(\mathbf{q})-\mathbf{f}(\mathbf{q}^{\mathrm{eq}})$. By inspection, this equilibrium-corrected equation can be solved in the usual manner (e.g. [33]). However, Eq. (3.6) does not suffer from the problems associated with conservation properties encountered previously. In calculating $\mathbf{h}^{*}$, if a steady equilibrium state is assumed preceding the simulation (e.g., for the SWEs, the water is motionless and in equilibrium), then $\partial/\partial t\to 0$, and so the original equation set can be reduced to

$$\int_{\Omega}\frac{\partial\mathbf{f}(\mathbf{q}^{\mathrm{eq}})}{\partial x}\,\mathrm{d}\Omega=\int_{\Omega}\mathbf{h}^{\mathrm{eq}}\,\mathrm{d}\Omega. \tag{3.7}$$

It is at this stage that the root cause of the numerical imbalance reveals itself, since within the discretisation scheme Eq. (3.7) does not hold, as seen in Section 2 for the special case of the shallow water equations. Approaches such as eigenvalue decomposition of the source terms [22] make the source terms effectively become pseudo flux terms. Herein, the imbalance is accepted, but is used as a means to derive a form of the governing equations that exploits the deviation from the system's unforced equilibrium (Eq. (3.6)) during the numerical solution process. This idea has a sound physical basis given that the motion of all dynamical systems can be viewed or analysed as being driven by external inputs and their position relative to their unforced equilibrium. Therefore, although the root cause of the numerical incompatibility is strictly still contained within the numerical scheme, as long as the deviations from the equilibrium are calculated correctly, the approach should nevertheless predict the system's behaviour properly.

From Eq. (3.7),

$$\mathbf{h}^{*}=\mathbf{h}-\mathbf{h}^{\mathrm{eq}}. \tag{3.8}$$

Hence, at each time step during the simulation the equilibrium source vector $\mathbf{h}^{\mathrm{eq}}$ is subtracted from $\mathbf{h}$. Alternatively, Eq. (3.6) can be derived by subtracting the equilibrium state of Eq. (3.1) from (3.1) itself.

3.2. Choice of solution technique

At this point there are two ways to solve Eqs. (3.3) or (3.6):

(a) Find $\int_{\Omega}(\partial\mathbf{f}(\mathbf{q}^{\mathrm{eq}}))/(\partial x)\,\mathrm{d}\Omega$ and $\mathbf{h}^{\mathrm{eq}}$ once only at the beginning of the simulation using Roe's approximate Riemann solver and then subtract them at each iteration in the evaluation of both sides of Eqs. (3.3) and (3.6).

(b) Alternatively, evaluate the equilibrium-corrected flux gradient term $\int_{\Omega}(\partial/\partial x)[\mathbf{f}(\mathbf{q})-\mathbf{f}(\mathbf{q}^{\mathrm{eq}})]\,\mathrm{d}\Omega$ using Roe's Riemann solver each time step and evaluate $\mathbf{h}^{*}=\mathbf{h}-\mathbf{h}^{\mathrm{eq}}$.

Method (a) is the most straightforward, but not necessarily the simplest. This depends on the equations and their simplicity at the initial equilibrium or 'still-water' state. Therefore, method (b) may offer some advantages depending on the complexity of the system of equations, and thus is subjected to a closer examination.

3.3. Invariance of the flux Jacobian

We consider method (b), and applying a quasi-linearisation to the following non-homogeneous system of equations,

$$\frac{\partial(\mathbf{q}' + \mathbf{q}^{\mathrm{eq}})}{\partial t} + \frac{\partial}{\partial x}[\mathbf{f}(\mathbf{q}) - \mathbf{f}(\mathbf{q}^{\mathrm{eq}})] = \mathbf{h}^*, \tag{3.9}$$

we get

$$\frac{\partial \mathbf{q}'}{\partial t} + \mathbf{A}' \frac{\partial(\mathbf{q} - \mathbf{q}^{\mathrm{eq}})}{\partial x} = \mathbf{h}^*, \tag{3.10}$$

where the equilibrium-corrected flux Jacobian $\mathbf{A}'$ (denoting element-by-element differentiation) is given by

$$\mathbf{A}' = \frac{\partial[\mathbf{f}(\mathbf{q}) - \mathbf{f}(\mathbf{q}^{\mathrm{eq}})]}{\partial(\mathbf{q} - \mathbf{q}^{\mathrm{eq}})} = \frac{\partial[\mathbf{f}(\mathbf{q}) - \mathbf{f}(\mathbf{q}^{\mathrm{eq}})]}{\partial \mathbf{q}'}. \tag{3.11}$$

Now, since $\partial \mathbf{f}(\mathbf{q}^{\mathrm{eq}})/\partial \mathbf{q}' = 0$, Eq. (3.11) reduces to

$$\mathbf{A}' = \frac{\partial \mathbf{f}(\mathbf{q})}{\partial \mathbf{q}'} = \frac{\partial \mathbf{f}(\mathbf{q})}{\partial \mathbf{q}} \frac{\partial \mathbf{q}}{\partial \mathbf{q}'}. \tag{3.12}$$

As $\mathbf{q} = \mathbf{q}^{\mathrm{eq}} + \mathbf{q}'$, then $\partial \mathbf{q}/\partial \mathbf{q}' = \mathbf{I}$ (the identity matrix), which is easily seen to be the case with the SWEs. Hence, Eq. (3.12) becomes

$$\mathbf{A}' = \frac{\partial \mathbf{f}(\mathbf{q})}{\partial \mathbf{q}} = \mathbf{A}, \tag{3.13}$$

which is exactly the case found with the SWEs in [33]. Unsurprisingly, Eq. (3.13) proves that the equilibrium-corrected flux Jacobian is exactly the same as the flux Jacobian for the conventional hyperbolic system. Depending on the complexity of the equation system being solved, $\mathbf{A}'$ may be very difficult to derive algebraically. However, from Eq. (3.13), it is clear that only the flux Jacobian for the conventional equations need be obtained. The SWEs are a simple and well-posed set of equations, so it is not surprising that $\mathbf{A}'$ can be derived easily as was shown by Rogers et al. It should also be noted that for the SWEs, the quiescent or still water state has the simple form $\zeta = u = v = 0$. However, this is not always the case with all equation systems as will be seen in Section 5.

An advantage of this approach over a posteriori numerical methods such as those developed by Vázquez-Cendón [38] and Hubbard and García-Navarro [22] is that the analysis is valid for arbitrary order of numerical approximation. It is also clear that the general principles are not restricted to Roe's approximate Riemann solver. This balancing methodology is not necessarily a more efficient approach but is a mathematically general treatment that overcomes a genuine problem that afflicts Roe's approximate solver when applied to hyperbolic equations.

4. Flux gradient and source balancing using shallow water equations

The generalised flux gradient and source term balancing technique will first be demonstrated with the SWEs since they provide one of the simplest examples of numerical imbalance. Herein, the solution methodology of Rogers et al. [33] is repeated briefly with extra salient points that were hitherto not realised.

4.1. Numerical discretisation

We write the two-dimensional SWEs (Eqs. (2.1a)–(2.1c)) in integral form as

$$\frac{\partial}{\partial t}\int_\Omega \mathbf{q}\,\mathrm{d}\Omega + \int_\Omega \left(\frac{\partial \mathbf{f}}{\partial x}+\frac{\partial \mathbf{g}}{\partial y}\right)\mathrm{d}\Omega = \int_\Omega \mathbf{h}\,\mathrm{d}\Omega, \tag{4.1}$$

where $\mathbf{g}$ is a flux vector. For the SWEs, the vectors $\mathbf{q}$, $\mathbf{f}$, $\mathbf{g}$ and $\mathbf{h}$ are conventionally given in hyperbolic form using the splitting Eq. (2.2)

$$\begin{aligned}
\mathbf{q} &= \begin{bmatrix} h \\ uh \\ vh \end{bmatrix}, \quad \mathbf{f} = \begin{bmatrix} uh \\ u^2h + \frac{1}{2}gh^2 - \varepsilon h\partial u/\partial x \\ uvh - \varepsilon h\partial v/\partial x \end{bmatrix}, \quad \mathbf{g} = \begin{bmatrix} vh \\ uvh - \varepsilon h\partial u/\partial y \\ v^2h + \frac{1}{2}gh^2 - \varepsilon h\partial v/\partial y \end{bmatrix} \quad \text{and} \\
\mathbf{h} &= \begin{bmatrix} 0 \\ (\tau_{wx} - \tau_{bx})/\rho - ghS_{ox} + hfv \\ (\tau_{wy} - \tau_{by})/\rho - ghS_{oy} - hfu \end{bmatrix}.
\end{aligned} \tag{4.2}$$

Recall that for 'still water' (or eq) values, the SWEs have the convenient properties $\zeta = u = v = 0$ and $h = h_s$, so that by applying the flux-gradient source-term balance of Section 3 (method b), these vectors are transformed to

$$\begin{aligned}
\mathbf{q}' &= \mathbf{q} - \mathbf{q}^{\mathrm{eq}} = \begin{bmatrix} \zeta \\ uh \\ vh \end{bmatrix}, \quad \mathbf{f}' = \mathbf{f} - \mathbf{f}^{\mathrm{eq}} = \begin{bmatrix} uh \\ u^2h + \frac{1}{2}g(\zeta^2 + 2\zeta h_s) - \varepsilon h\partial u/\partial x \\ uvh - \varepsilon h\partial v/\partial x \end{bmatrix}, \\
\mathbf{g}' &= \mathbf{g} - \mathbf{g}^{\mathrm{eq}} = \begin{bmatrix} vh \\ uvh - \varepsilon h\partial u/\partial y \\ v^2h + \frac{1}{2}g(\zeta^2 + 2\zeta h_s) - \varepsilon h\partial v/\partial y \end{bmatrix}, \quad \mathbf{h}^* = \mathbf{h} - \mathbf{h}^{\mathrm{eq}} = \begin{bmatrix} 0 \\ (\tau_{wx} - \tau_{bx})/\rho - g\zeta S_{ox} + hfv \\ (\tau_{wy} - \tau_{by})/\rho - g\zeta S_{oy} - hfu \end{bmatrix}.
\end{aligned} \tag{4.3}$$

These are exactly the same vectors used by Rogers et al. [33], who utilised the slightly different approach of algebraic manipulation of Eq. (2.2) to obtain Eq. (2.12).

Using the flux-gradient and source-term balance and applying Gauss' theorem to the flux gradient integral, Eq. (4.1) may be written as

$$\frac{\partial}{\partial t}\int_\Omega \mathbf{q}'\,\mathrm{d}\Omega + \oint_S \left(\hat{\mathbf{f}} - \hat{\mathbf{f}}^{\mathrm{eq}}\right)\mathrm{d}S = \int_\Omega \mathbf{h}^*\,\mathrm{d}\Omega, \tag{4.4}$$

where $\hat{\mathbf{f}}$ is the vector of flux functions through S given by

$$\hat{\mathbf{f}} = \mathbf{f}n_x + \mathbf{g}n_y, \tag{4.5}$$

in which n_x and n_y are the Cartesian components of $\mathbf{n}$, the unit normal vector to S. In Eq. (4.4), $\hat{\mathbf{f}} - \hat{\mathbf{f}}^{\mathrm{eq}} = \hat{\mathbf{f}}'$ may also be written in terms of inviscid and viscous fluxes as

$$\hat{\mathbf{f}}' = \mathbf{f}^{\mathrm{I}} - \varepsilon \mathbf{f}^{\mathrm{V}}, \tag{4.6}$$

where

$$\mathbf{f}^{\mathrm{I}} = \begin{bmatrix} uhn_x + vhn_y \\ (u^2h + g[\zeta^2 + 2\zeta h_s]/2)n_x + uvhn_y \\ uvhn_x + (v^2h + g[\zeta^2 + 2\zeta h_s]/2)n_y \end{bmatrix} \quad \text{and} \quad \mathbf{f}^{\mathrm{V}} = \begin{bmatrix} 0 \\ (h\partial u/\partial x)n_x + (h\partial u/\partial y)n_y \\ (h\partial v/\partial x)n_x + (h\partial v/\partial y)n_y \end{bmatrix}. \tag{4.7}$$

The equations are discretised on a collocated grid with ζ, uh and vh stored at the centre of each cell. For each cell, Eq. (4.4) can be more conveniently rewritten as

$$\left.\frac{\partial V \mathbf{q}'}{\partial t}\right|_i = -\oint_{\partial C_i} \left(\hat{\mathbf{f}} - \hat{\mathbf{f}}^{\mathrm{eq}}\right) \mathrm{d}S + V_i\left(\mathbf{h}_i - \mathbf{h}_i^{\mathrm{eq}}\right) = -\oint_{\partial C_i} \hat{\mathbf{f}}_i' \,\mathrm{d}S + V_i \mathbf{h}_i^*. \tag{4.8}$$

The surface integral in Eq. (4.8) can be evaluated in discrete form by using $\oint_{\partial C_i} \hat{\mathbf{f}}_i' \,\mathrm{d}s = (\hat{\mathbf{f}}_{\mathrm{E}}' - \hat{\mathbf{f}}_{\mathrm{W}}' + \hat{\mathbf{f}}_{\mathrm{N}}' - \hat{\mathbf{f}}_{\mathrm{S}}')\,\Delta s$, where $\hat{\mathbf{f}}_{\mathrm{E}}'$, $\hat{\mathbf{f}}_{\mathrm{W}}'$, $\hat{\mathbf{f}}_{\mathrm{N}}'$ and $\hat{\mathbf{f}}_{\mathrm{S}}'$ are the vector fluxes through the east, west, south and north faces of each cell, and Δs is the length of the side of the cell. At each cell edge, the convective fluxes are evaluated using Roe's Riemann solver (Eq. (2.8)). Eq. (4.8) is then integrated in time using the second-order Adams–Bashforth scheme.

As proven in Section 3.3, the inviscid flux Jacobian remains unchanged and is given by

$$\mathbf{A} = \frac{\partial(\mathbf{f}^{\mathrm{I}})}{\partial \mathbf{q}} = \begin{bmatrix} 0 & n_x & n_y \\ (c^2 - u^2)n_x - uvn_y & 2un_x + vn_y & un_y \\ -uvn_x + (c^2 - v^2)n_y & vn_x & un_x + 2vn_y \end{bmatrix}, \tag{4.9}$$

which has real and distinct eigenvalues (confirming hyperbolicity),

$$\lambda_1 = un_x + vn_y, \quad \lambda_2 = un_x + vn_y - cn, \quad \lambda_3 = un_x + vn_y + cn, \tag{4.10}$$

where c is the wave celerity and $n = \sqrt{n_x^2 + n_y^2} = 1$. The associated right and left eigenvector matrices are

$$\mathbf{R} = \begin{bmatrix} 0 & 1 & 1 \\ n_y & u - (cn_x/n) & u + (cn_x/n) \\ -n_x & v - (cn_y/n) & v + (cn_y/n) \end{bmatrix} \quad \text{and} \quad \mathbf{L} = \begin{bmatrix} -\frac{(un_y - vn_x)}{n^2} & \frac{n_y}{n^2} & -\frac{n_x}{n^2} \\ \frac{1}{2} + \frac{un_x + vn_y}{2cn} & \frac{-n_x}{2cn} & \frac{-n_y}{2cn} \\ \frac{1}{2} - \frac{un_x + vn_y}{2cn} & \frac{n_x}{2cn} & \frac{n_y}{2cn} \end{bmatrix}. \tag{4.11}$$

These eigenvalues and eigenvectors also confirm that the approach in Section 3 ensures the still-water corrected SWEs retain their hyperbolic nature, which is a prerequisite for using Roe's approximate Riemann solver. It is no surprise, therefore, that the shock propagation speed given by the flux-gradient source-term balanced SWEs has the same theoretical result as that given by Toro [36].

The variables u, v, c in Eqs. (4.9)–(4.11) are given by Roe's average state which is defined as

$$u = \frac{u^+\sqrt{h^+} + u^-\sqrt{h^-}}{\sqrt{h^+} + \sqrt{h^-}}, \quad v = \frac{v^+\sqrt{h^+} + v^-\sqrt{h^-}}{\sqrt{h^+} + \sqrt{h^-}} \quad \text{and} \quad c = \sqrt{\frac{g(h^+ + h^-)}{2}}, \tag{4.12}$$

where the superscripts + and − denote the right and left Riemann states on either side of a cell interface, respectively.

A nonlinear slope limiter is used to prevent unphysical oscillations and render the scheme total variation diminishing (TVD). Herein, the limiter is implemented such that, for consecutive cells $i-1$, i, $i+1$ on a locally uniform grid, the reconstructed Riemann states are given by

$$q^{-}_{i+\frac{1}{2}} = q_i + \frac{\Phi}{2}(q_i - q_{i-1}) \quad \text{and} \quad q^{+}_{i-\frac{1}{2}} = q_i - \frac{\Phi}{2}(q_i - q_{i-1}), \tag{4.13}$$

where Φ is the limiter. In practice, the limiter restricts the gradient such that the cell face data, reconstructed from the stored cell-centre values, fall within the range of the cell-centre data in the cells either side of the interface. As given by Hirsch [20], Φ is defined as

$$\Phi(r) = \max[0, \min(\beta r, 1), \min(r, \beta)], \tag{4.14}$$

where the limiter parameter $1 \leqslant \beta \leqslant 2$, and the gradient ratio is given by

$$r = \begin{cases} \frac{q_{i+1}-q_i}{q_i-q_{i-1}}, & q_i - q_{i-1} \neq 0, \\ 0, & q_i - q_{i-1} = 0. \end{cases} \tag{4.15}$$

The choice of minmod slope limiter ($\beta = 1$) used herein is of relatively low strength and so is slightly dissipative, but this effect should not be overly significant for shallow water flows (see [3]). Finally, the entropy fix of Harten and Hyman [19] is used to avoid the numerical solution generating unphysical discontinuities.

4.2. Numerical results for shallow water equations

4.2.1. Choice of validation tests

Any flux-gradient and source-term balancing scheme must be able to deal with the flow regimes present in shallow water flows over varying bathymetries. A balancing technique must therefore address the following [22]:

(i) The ability to maintain quiescent flow.
(ii) The accuracy of approximations to both continuous and discontinuous steady state solutions.
(iii) The accuracy of simple time-dependent approximations.

LeVeque [24] devised several benchmark tests including steady transcritical flow over a one-dimensional hump and the propagation of free surface disturbances over one- and two-dimensional humps. Hubbard and García-Navarro [22] and Zhou et al. [41] validated their models using LeVeque's test cases, as well as tidal wave flow cases suggested by Vázquez-Céndon [38]. These included shallow subcritical flows in channels of variable width and changing bed slope, where asymptotic analytical solutions exist. Zhou et al. [41] simulated bore reflection in a diverging channel and compared numerical predictions with experimental results for a hydraulic jump. The Working Group on Dam Break Modelling [18] proposed standard tests, which include many of the above cases, with particular emphasis on comparisons with well documented experimental data and analytical solutions.

Of the cases that emphasise problems involving the issues mentioned above, we select the following tests:

(i) Wind-induced flow in a circular basin of non-uniform bathymetry.
(ii) Steady transcritical flow over a one-dimensional hump.
(iii) Wave propagation over a two-dimensional hump.

It has been shown that the formulation accurately predicts standard dam break cases (see Borthwick et al. [7]), confirming that the proposed balancing technique does indeed preserve the shock capturing property of Roe's Riemann solver embedded in a Godunov-type scheme.

4.2.2. Wind-induced circulation in a circular basin

Consider the circular dish-shaped shallow flow domain where numerical incompatibility of conventional shallow water formulations was demonstrated in Section 2. An eastward-directed uniform surface stress of 0.02 N/m^2 is built up over 1000 s, with a time step of 0.05 s. The Coriolis force is set to zero and the eddy viscosity coefficient is 0.00012 m^2/s. Bed friction is given by a logarithmic relationship such that

$$\tau_{bx} = C_D \rho u \sqrt{u^2 + v^2} \quad \text{and} \quad \tau_{by} = C_D \rho v \sqrt{u^2 + v^2}, \tag{4.16}$$

where [34]

$$C_D = \left[\frac{\kappa}{B + \ln(z_0/h)} \right]^2, \tag{4.17}$$

the von Kármán constant $\kappa = 0.4$, the integration parameter $B = 1$, the bed roughness height $z_0 = 2.8$ mm and h is the total water depth. Fig. 3 depicts the depth-averaged velocities and stream function contours within the dish at $t = 10,000$ s, when steady state was achieved. The flow is directed against the wind along the east–west axis of the dish, and there are two counter-rotating gyres with their centres located slightly downstream of the middle of the basin, in close agreement with the analytical model of Kranenburg [23] and identical to the results presented by Rogers et al. [33]. This confirms that a physically meaningful flow field is produced using the new balanced hyperbolic matrix formulation.

4.2.3. Steady-transcritical flow with a shock over a one-dimensional hump

This benchmark test (see [38,41]) comprises flow along a 25 m long one-dimensional channel with a bump defined by

$$h_s = \begin{cases} 0.05(x - 10)^2 & \text{if } 8 \text{ m} < x < 12 \text{ m}, \\ 0.2 & \text{otherwise}, \end{cases} \tag{4.18}$$

where x is the distance along the channel. The boundary conditions determine the flow conditions which can be subcritical, transcritical with or without a shock, or supercritical. Analytical solutions are provided by Goutal and Maurel [18]. In the present paper, the boundary conditions have been chosen to induce transcritical flow with a shock over the hump, as this is the most demanding for a numerical scheme when predicting a steady discontinuous solution over a non-uniform bathymetry. Thus, the discharge per unit depth at the upstream boundary is specified as $q = 0.18$ m^2/s and the depth at the downstream boundary is

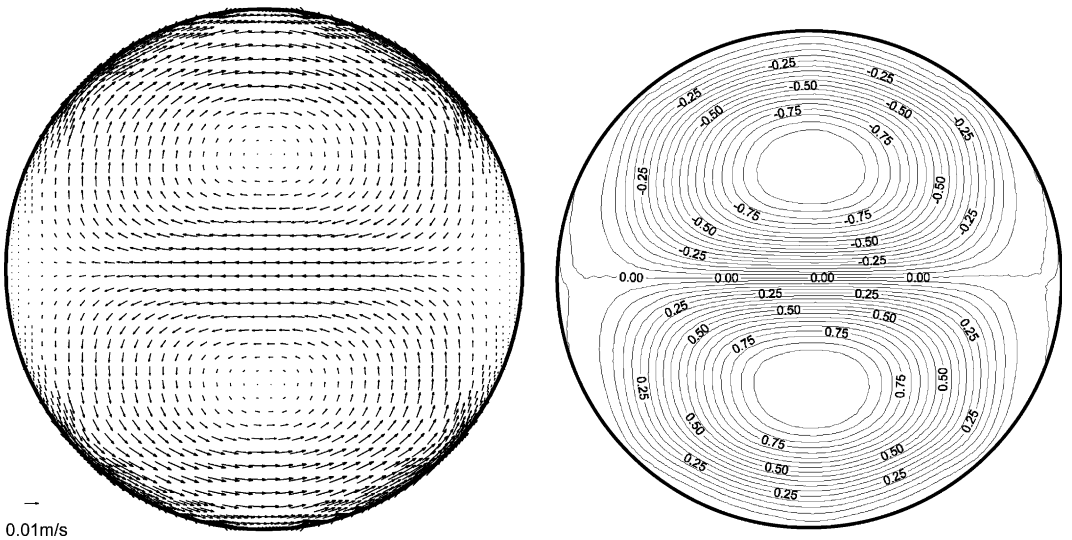

Fig. 3. Circular basin: wind-induced circulation.

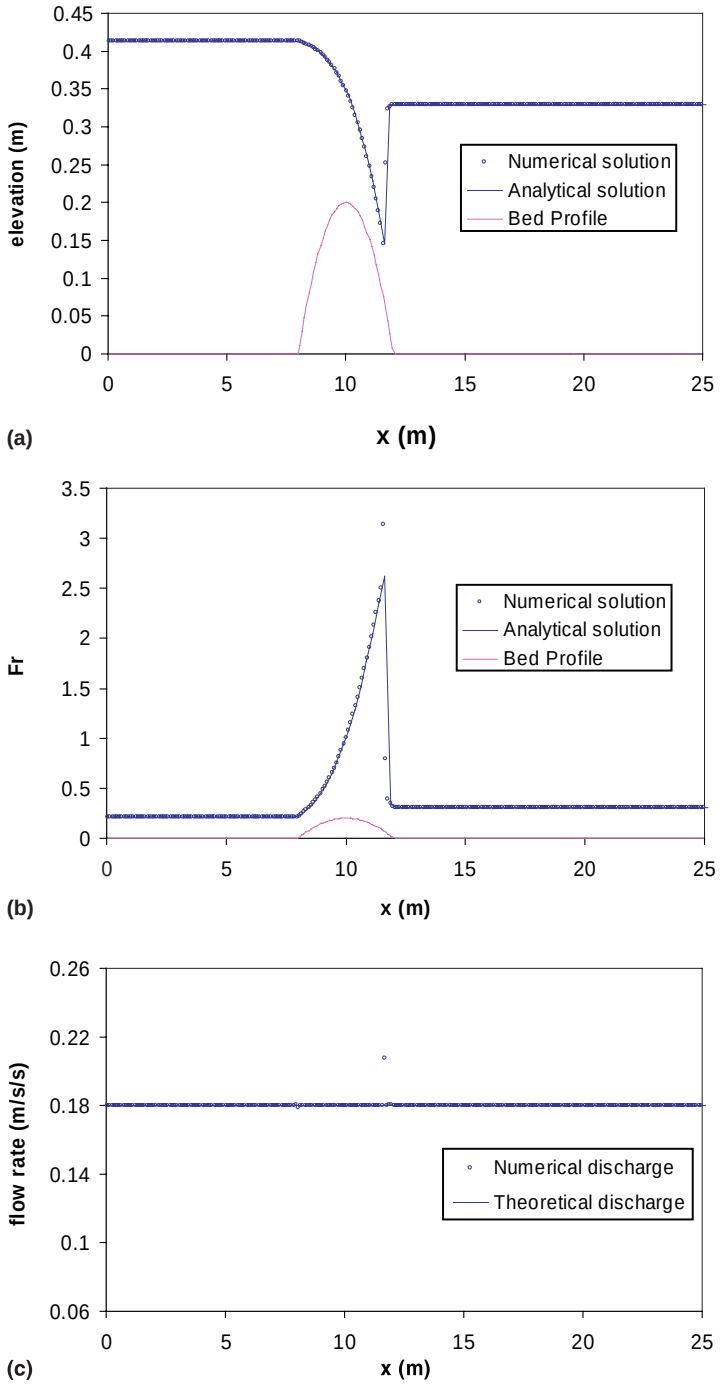

Fig. 4. Steady transcritical flow over a hump with a shock: (a) Water surface elevation. (b) Froude number. (c) Comparison of discharge.

$h = 0.33$ m. The numerical domain is uniformly discretised in space using 256 cells. The time step Δt is 0.0175 s. The bed is frictionless and there is no eddy viscosity.

Fig. 4 shows the converged steady-state numerical predictions of the water depth, Froude number and discharge along the channel. The agreement between the numerical prediction and the analytical solution is very close. The only significant deviation between the numerical and analytical solutions is in the flow rate at the location of the shock. This may also be observed in the results reported elsewhere [22,38,41]. This is surprising because the flow rate $q = uh$ is a quantity that should be conserved. However, little attention has been drawn to this discrepancy in the literature. The underlying reason may be due to the fact that Godunov-type methods do not conserve energy in this type of discontinuous shallow flow.

To assess convergence, a global relative error is defined [41] as

$$R = \sqrt{\sum_i \left(\frac{h_i^n - h_i^{n-1}}{h_i^n} \right)^2}, \tag{4.19}$$

where h^n and h^{n-1} are the water depths at time levels n and $n-1$, and the scheme is judged to have converged when $R < 5 \times 10^{-6}$. Fig. 5 shows the convergence history of the computed water depths. The solution has reached steady state by 3750 iterations according to the above criterion. When comparing different schemes, it must be remembered that the convergence history will depend on the time-integration scheme used.

4.2.4. Wave propagation over a two-dimensional hump

The two-dimensional bed topography proposed by LeVeque [24] is

$$h_s = 1 - \frac{1}{2} \exp\left[-50 \left(\left(x - \frac{1}{2} \right)^2 + \left(y - \frac{1}{2} \right)^2 \right) \right] \tag{4.20}$$

for $0 < x, y < 1$ m. Initial conditions are quiescent with $u = v = 0$ m/s and a free surface disturbance given by

$$\zeta = \begin{cases} 0.2 & \text{if } 0.1 \text{ m} < x < 0.2 \text{ m}, \\ 0 & \text{otherwise.} \end{cases} \tag{4.21}$$

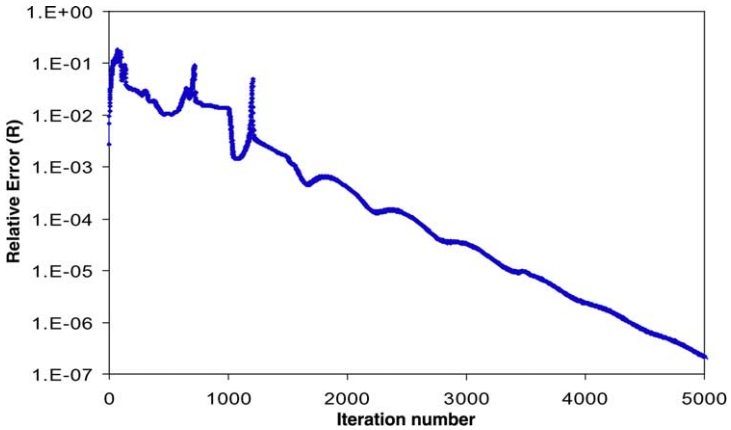

Fig. 5. Steady transcritical flow over a hump: convergence history.

At time $t = 0$ s, the water surface splits into two waves, each propagating with characteristic velocities $\pm\sqrt{gh}$, so that one wave leaves the domain and the other propagates over the hump. To achieve this, transmissive open boundaries (see [21]) are located at $x = 0$ and 1 m, and lateral slip boundaries at $y = 0$ and 1 m. A 100×100 uniform grid is used and the time increment is $\Delta t = 0.002$ s. Bed friction and viscosity are zero, and g is set at 1 m/s^2. Fig. 6 displays the water surface elevation at time $t = 0.7$ s by means of a

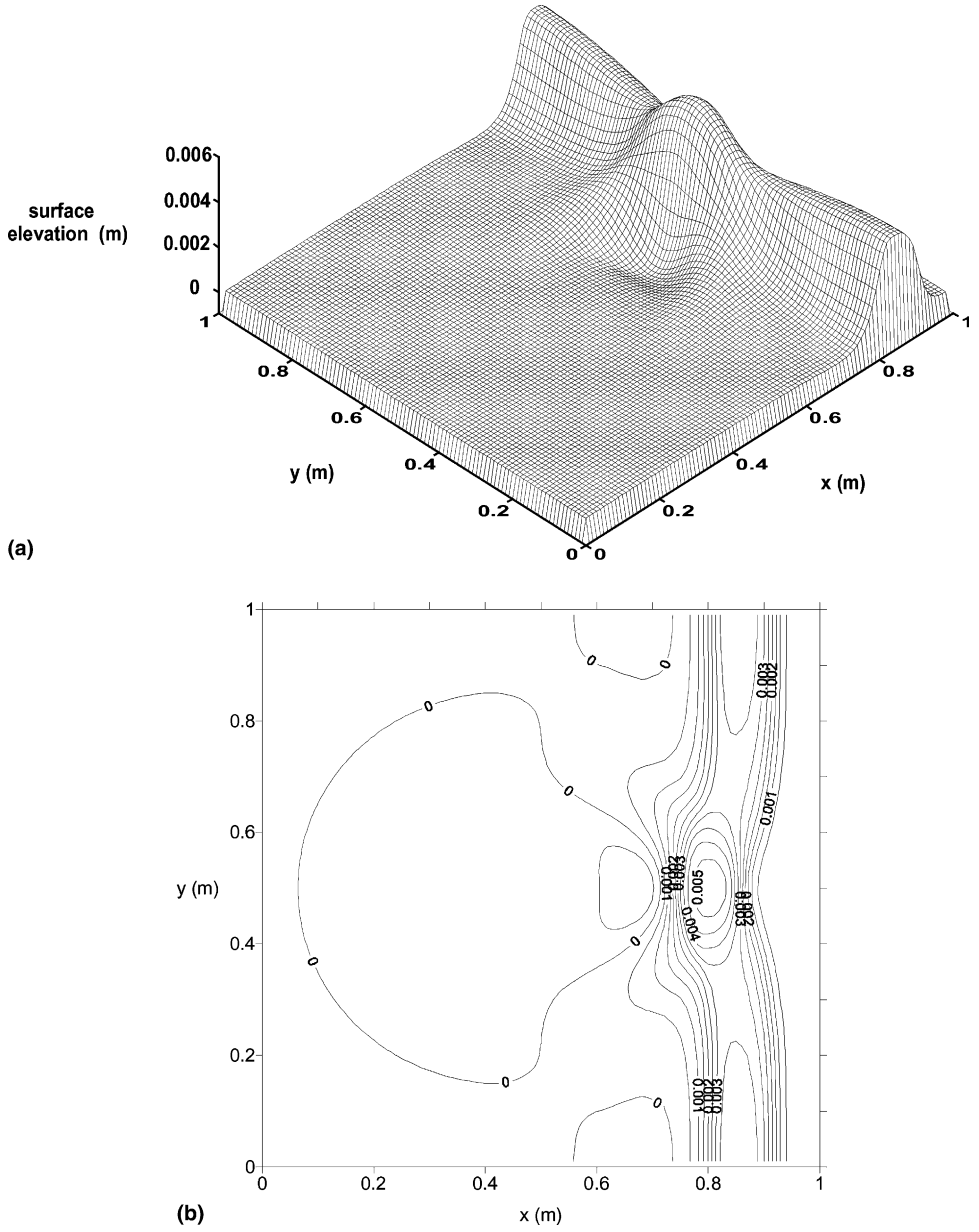

Fig. 6. Flow over a two-dimensional hump: (a) Three-dimensional view of water surface at $t = 0.7$ s. (b) Water surface contours (m) at $t = 0.7$ s.

three-dimensional surface plot and contour plot. The results show that the initial disturbance has propagated over the spatially varying bathymetry and concentrated the wave energy just behind the shoal. The plots indicate that unphysical numerical perturbations are not present in the solution and agree closely with the results obtained by LeVeque [24] and Hubbard and García-Navarro [22].

5. Demonstration of flux-gradient and source-term balancing using period-averaged wave–current interaction model

Many flux-gradient and source-term balancing techniques have been validated solely for the shallow water equations where the only terms that need alteration are those expressing the effect of bed slope. In this section, the new flux-gradient source-term balancing technique is applied to a more complicated set of equations arising in coastal engineering. These describe the period- and depth-averaged conservation of mass, momentum, wave energy and wave number in the nearshore zone [39]. A detailed numerical solver has already been presented for this equation system by Rogers et al. [32], which is briefly summarised herein.

5.1. Governing equations

As waves enter the coastal zone, they are modified by the bathymetry through reflection, refraction, diffraction and wave breaking, and are further altered by interaction with currents. The physical processes are extremely complex and, from the modelling perspective, require considerable idealisation. In the ray-type approach, which describes wave–current interaction and diffraction effects, it is assumed that vertical motions are negligible, pressure is hydrostatic, and that waves are progressive with no reflection. Hence, modified shallow water equations are derived by depth-averaging the Reynolds equations that conserve mass and momentum, which after including the effect of short waves and averaging over one wave period, may be written as:

$$\frac{\partial \eta}{\partial t} + \frac{\partial (uh)}{\partial x} + \frac{\partial (vh)}{\partial y} = 0, \tag{5.1a}$$

$$\frac{\partial (uh)}{\partial t} + \frac{\partial (u^2 h)}{\partial x} + \frac{\partial (uvh)}{\partial y} - \left(\varepsilon_x \frac{\partial (hu_x)}{\partial x} + \varepsilon_y \frac{\partial (hu_y)}{\partial y} \right) = \frac{\tau_{wx} - \rho g h \frac{\partial \eta}{\partial x}}{\rho}$$

$$\frac{\partial K_x}{\partial t} + \left(u + C_{gx}\right)\frac{\partial K_x}{\partial x} + \left(v + C_{gy}\right)\frac{\partial K_x}{\partial y} + S_h\frac{\partial h}{\partial x} + K_x\frac{\partial u}{\partial x} + K_y\frac{\partial v}{\partial x} - \frac{C_g}{2k}\frac{\partial \delta^*}{\partial x} = 0, \tag{5.2b}$$

$$\frac{\partial K_y}{\partial t} + \left(u + C_{gx}\right)\frac{\partial K_y}{\partial x} + \left(v + C_{gy}\right)\frac{\partial K_y}{\partial y} + S_h\frac{\partial h}{\partial y} + K_x\frac{\partial u}{\partial y} + K_y\frac{\partial v}{\partial y} - \frac{C_g}{2k}\frac{\partial \delta^*}{\partial y} = 0, \tag{5.2c}$$

where η is the period-averaged mean water level (set-up and set-down) above the still water level h_s, $h(=\eta + h_s)$ is the mean water depth, u and v are period- and depth-averaged velocities in the x- and y-directions, respectively, (u_x, u_y) and (v_x, v_y) are the spatial derivatives of (u, v), ρ is water density, τ_{wx} and τ_{wy} are surface stresses, τ_{bx} and τ_{by} are bed friction stresses, f is the Coriolis parameter, ϵ_x and ϵ_y are the kinematic eddy viscosity coefficients, $E = \rho g a^2/2$ is the wave energy per wave per unit crest length, a is the wave amplitude, K_x and K_y are the wave number components, C_g is the magnitude of the intrinsic group celerity with components C_{gx} and C_{gy}, k is the separation factor, C^a is a bottom friction coefficient related to the wave amplitude, S_h is a depth-related frequency response factor, and S_{xx}, S_{xy}, S_{yx} and S_{yy} are radiation stress components representing excess momentum flux due to waves.

The radiation stress tensor is given by

$$S_{ij} = \frac{1}{2}\left[(1+G)\frac{K_i}{k}\frac{K_j}{k} + G\delta_{ij}\right]E, \tag{5.3}$$

in which $G = 2kh/\sinh(2kh)$, δ_{ij} is the Kronecker delta ($\delta_{ij} = 1$ if $i = j$ and $\delta_{ij} = 0$ if $i \neq j$). The separation factor k is related to the wave number through the Battjes relation [4], $K^2 = k^2 + \delta^* = k^2(1+\delta)$, where $\delta^* = (1/a)\nabla^2 a = k^2\delta$ and δ is the diffraction factor. In tensor notation, the group celerity components are

$$C_{gi} = \frac{K_i}{k}C_g = \frac{1}{2}(1+G)\frac{\sigma_o}{k}\frac{K_i}{k} = \frac{1}{2}(1+\delta)(1+G)\frac{\sigma_o}{K}\frac{K_i}{K}, \tag{5.4}$$

where the group celerity is $C_g = (1+G)\sigma_o/(2k) = kG^K$, the intrinsic wave frequency is $\sigma_o = \sqrt{kg\tanh kh}$ and the wave number vector magnitude is $K = |\mathbf{K}| = \sqrt{K_x^2 + K_y^2}$, wherein $K_x = K\cos\theta$ and $K_y = K\sin\theta$. The depth-related frequency response factor is $S_h = \partial\sigma_o/\partial h = G\sigma_o/2h$. The final terms in Eqs. (5.2a)–(5.2c) model diffraction due to amplitude curvature of linear waves. The friction coefficient C^a, the kinematic eddy viscosity coefficients ϵ_x and ϵ_y and wave breaking are all estimated empirically using Bijker's [6], Thornton's [35] and the US-CERC [37] formula, respectively. More sophisticated closure sub-models could be utilised but are not implemented here, as the purpose of this paper is to implement flux-gradient and source term balancing with Roe's solver.

5.2. Numerical discretisation

Comparison of the depth- and period-averaged mass and momentum equations (5.1a)–(5.1c) with the SWEs of Section 2 (Eqs. (2.1a)–(2.1c)) reveals that the only real differences between the two formulations are the additional radiation stress gradients. Thus, Eqs. (5.1a)–(5.1c) can be classified as modified shallow water equations (MSWEs) while Eqs. (5.2a)–(5.2c) are classified as wave conservation equations (WCEs). Given that the solver of Rogers et al. [33] has already been shown to be a fully validated numerical scheme for the SWEs, the same approach is used for the wave-induced currents by treating the radiation stress gradient terms as additional source terms using Roe's approximate Riemann solver for the MSWEs and WCEs convective fluxes in a second-order Godunov-type scheme. For the MSWEs, the vectors **q**, **f**, **g** and **h** are given by

$$\mathbf{q} = \begin{bmatrix} h \\ uh \\ vh \end{bmatrix}, \quad \mathbf{f} = \begin{bmatrix} uh \\ u^2h + \frac{1}{2}gh^2 - \varepsilon h\partial u/\partial x \\ uvh - \varepsilon h\partial v/\partial x \end{bmatrix}, \quad \mathbf{g} = \begin{bmatrix} vh \\ uvh - \varepsilon h\partial u/\partial y \\ v^2h + \frac{1}{2}gh^2 - \varepsilon h\partial v/\partial y \end{bmatrix} \quad \text{and}$$
$$\mathbf{h} = \begin{bmatrix} 0 \\ \frac{\tau_{wx}-\tau_{bx}}{\rho} - ghS_{ox} + hfv - \frac{1}{\rho}\left(\frac{\partial S_{xx}}{\partial x} + \frac{\partial S_{xy}}{\partial y}\right) \\ \frac{\tau_{wy}-\tau_{by}}{\rho} - ghS_{oy} - hfu - \frac{1}{\rho}\left(\frac{\partial S_{yx}}{\partial x} + \frac{\partial S_{yy}}{\partial y}\right) \end{bmatrix}. \tag{5.5}$$

For the WCEs, the vectors are

$$\mathbf{q} = \begin{bmatrix} E \\ K_x \\ K_y \end{bmatrix}, \quad \mathbf{f} = \mathbf{f}^{\mathrm{W}} + \mathbf{f}^{\mathrm{WCI}} = \begin{bmatrix} EC_{gx} \\ \sigma_o \\ 0 \end{bmatrix} + \begin{bmatrix} uE \\ uK_x + vK_y \\ 0 \end{bmatrix} = \begin{bmatrix} EC_{gx} + uE \\ \sigma_o + uK_x + vK_y \\ 0 \end{bmatrix},$$
$$\mathbf{g} = \mathbf{g}^{\mathrm{W}} + \mathbf{g}^{\mathrm{WCI}} = \begin{bmatrix} EC_{gy} \\ 0 \\ \sigma_o \end{bmatrix} + \begin{bmatrix} vE \\ 0 \\ uK_x + vK_y \end{bmatrix} = \begin{bmatrix} EC_{gy} + vE \\ 0 \\ \sigma_o + uK_x + vK_y \end{bmatrix} \quad \text{and} \tag{5.6}$$
$$\mathbf{h} = \begin{bmatrix} -\left(S_{xx}\frac{\partial u}{\partial x} + S_{xy}\frac{\partial u}{\partial y} + S_{yx}\frac{\partial v}{\partial x} + S_{yy}\frac{\partial v}{\partial y}\right) - \rho gaC^a a^2 + \frac{\rho ga}{2}\left(\varepsilon_x\frac{\partial^2 a}{\partial x^2} + \varepsilon_y\frac{\partial^2 a}{\partial y^2}\right) \\ -C_{gy}\frac{\partial K_x}{\partial y} - S_h\frac{\partial h_s}{\partial x} + \frac{C_g}{2k}\frac{\partial \delta^*}{\partial x} \\ -C_{gx}\frac{\partial K_y}{\partial x} - S_h\frac{\partial h_s}{\partial y} + \frac{C_g}{2k}\frac{\partial \delta^*}{\partial y} \end{bmatrix},$$

where superscripts W and WCI refer to wave and wave–current interaction fluxes (see [32]). Using flux gradient and source term balancing, both the MSWEs and WCEs may be written in the form of Eqs. (4.4) and (4.8). The equations are discretised on a collocated grid with E, K_x, K_y, η, uh and vh stored at the centre of each cell.

For the MSWEs, the inviscid flux Jacobian and its eigenvectors remain identical (Eqs. (4.10)–(4.12)). For the WCEs, the flux Jacobian is given by [32]

$$\mathbf{A} = \frac{\partial\left(\mathbf{f}^{\mathrm{W}} + \mathbf{g}^{\mathrm{W}}\right)}{\partial \mathbf{q}}$$
$$= \begin{bmatrix} C_{gx}n_x + C_{gy}n_y & \left(K_x\frac{\partial G^K}{\partial K_x} + G^K\right)En_x + K_y\frac{\partial G^K}{\partial K_x}En_y & K_x\frac{\partial G^K}{\partial K_y}En_x + \left(K_y\frac{\partial G^K}{\partial K_y} + G^K\right)En_y \\ 0 & \left(C_{gx} + S_h\frac{\partial \eta}{\partial K_x}\right)n_x & 0 \\ 0 & 0 & \left(C_{gy} + S_h\frac{\partial \eta}{\partial K_y}\right)n_y \end{bmatrix}, \tag{5.7}$$

where

$$G^K = \frac{C_g}{k}, \quad \frac{\partial G^K}{\partial K_i} = \frac{\partial G^K}{\partial k}\frac{\partial k}{\partial K_i}$$

and

$$\frac{\partial G^K}{\partial k} = -\frac{\sigma_o}{k^3}\left[1 + \frac{G}{2}\left(1 + \frac{2kh}{\tanh 2kh}\right)\right] + \frac{C_g^2}{\sigma_o k}. \tag{5.8}$$

For the WCEs, **A** has eigenvalues given by

$$\lambda_1 = C_{gx}n_x + C_{gy}n_y, \quad \lambda_2 = C_{gx}n_x + S_h\frac{\partial\eta}{\partial K_x}n_x, \quad \lambda_3 = C_{gy}n_y + S_h\frac{\partial\eta}{\partial K_y}n_y. \tag{5.9}$$

The associated right and left eigenvector matrices are

$$\mathbf{R} = \begin{bmatrix} 1 & A_{12} & A_{13} \\ 0 & S_h\frac{\partial\eta}{\partial K_x}n_x & 0 \\ 0 & 0 & S_h\frac{\partial\eta}{\partial K_y}n_y \end{bmatrix} \quad \text{and} \quad \mathbf{L} = \begin{bmatrix} 1 & -A_{12}\left(S_h\frac{\partial\eta}{\partial K_x}n_x\right)^{-1} & -A_{13}\left(S_h\frac{\partial\eta}{\partial K_y}n_y\right)^{-1} \\ 0 & \left(S_h\frac{\partial\eta}{\partial K_x}n_x\right)^{-1} & 0 \\ 0 & 0 & \left(S_h\frac{\partial\eta}{\partial K_y}n_y\right)^{-1} \end{bmatrix}. \tag{5.10}$$

When solving these equations, the initial values of the wave number components are estimated from the linear dispersion equation, $\sigma_o = \sqrt{kg\tanh kh}$, and Snell's Law, and these wave number component values change slightly as the solution evolves. Note also that for non-diffractive simulations, amplitude curvature due to diffraction is negligible so that δ^* and its gradients are set to zero. Hence, the solution is advanced by evaluating the surface integral in Eq. (4.8) using the same procedure detailed in Section 4.1, and then similarly integrating in time using a second-order Adams–Bashforth scheme.

This formulation involves a similar splitting of terms between flux gradients and source terms to that used for the SWEs to ensure hyperbolicity. In this case,

$$S_h\frac{\partial h}{\partial x} = S_h\frac{\partial\eta}{\partial x} + S_h\frac{\partial h_s}{\partial x}, \tag{5.11}$$

which will test the ability of the proposed balancing scheme to deal with a different but related problem. The quiescent or still-water state for the combined MSWEs and WCEs is defined as $\eta = u = v = 0$, $h = h_s$, $E = 0$, $K_x = K_y = 0$, but $k \neq 0$ since the frequency σ is specified over the whole domain.

5.3. Numerical results for period-averaged wave–current interaction model

5.3.1. Wave flow over a stepped bathymetry

The WCEs describe the wave transformation over a gradually varying bathymetry, and therefore they describe changes in the wave parameters as waves pass over a mildly sloping bottom. Hence, the equations are not derived with the aim of simulating discontinuous flows, but rather gradually varying ones. However, it is interesting to see the numerical results obtained when applied to such a case. The test proposed here consists of a one-dimensional channel of length 4 m with a sudden step in the centre defined by

$$h_s = \begin{cases} 0.9 - 0.2x, & 0 < x < 2\text{m}, \\ 0.26 - 0.08(x-2), & 2\text{m} < x < 4\text{m}, \end{cases} \tag{5.12}$$

where x is the distance along the channel. In reality such a sudden change in the bed would generate not only a sudden change in the wave parameters, but the waves would produce currents in the vicinity of the step (in addition to those being generated as the waves progress up the sloping beach), which would in turn have a feedback effect on the wave parameters. This essentially makes an analytical solution impossible (hence the need for a numerical scheme). However, for the purposes of model evaluation, wave–current interaction is removed to create an idealised case for which an analytical solution can be derived by solving the linear dispersion relation at local water depths when calculating the shoaling wave heights (see [12]).

The numerical domain is discretised spatially using a uniform grid of 64 cells with $\Delta x = 0.0625$ m. The time step is $\Delta t = 0.01$ s. Eddy viscosity and bed friction are neglected. The wave number K_x is initially set to an arbitrary value of 2.5 rad/m along the length of the channel. The initial wave height is zero everywhere, except at the inlet where the wave height is equal to 0.02 m.

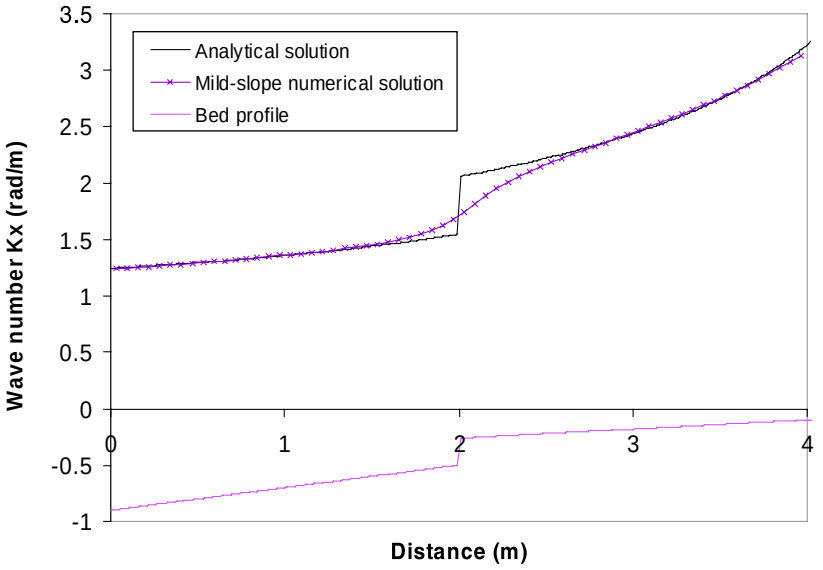

Fig. 7. One-dimensional wave flow over a step: wave number predictions for mild slope solution.

Fig. 7 shows the analytical solution and numerical solution of the wave number K_x for an assumed mild-slope over the stepped bathymetry. While there is no unphysical numerical oscillation present, the nature of the governing equations has been to smooth out any discontinuity in the wave number induced by the stepped-bathymetry. To cure this, an additional flux is required, namely

$$\mathbf{f} = \begin{bmatrix} \frac{ES_h}{k}\left(\frac{3}{2} + \frac{G}{2} - \frac{2kh}{\tanh 2kh}\right) \\ S_h n_x \\ S_h n_y \end{bmatrix} \Delta h_s, \tag{5.13}$$

to account for a sudden change in the bed. When Eq. (5.13) is included, the agreement between the numerical and analytical solutions is excellent as shown in Fig. 8. The agreement for wave height (not shown here) along the channel is also excellent.

Fig. 9 illustrates the convergence history, where the global relative error defined by Eq. (4.19) is calculated with water depth replaced by wave number. Using the criterion given in Section 4.2.4, convergence occurs by 8000 iterations. It is important to note here that, in the absence of flux gradient and source term balancing, the scheme is unstable. Such behaviour will be shown in more detail for the next two cases.

5.3.2. Wave diffraction over a submerged elliptical shoal

Berkhoff et al. [5] presented laboratory data for waves diffracting over a submerged elliptical shoal on a plane beach. This has become a standard benchmark test to verify numerical wave models (e.g. [25,26]). Here, only weak currents are generated making it ideal for testing the effectiveness of flux-gradient and source term balancing in the wave conservation equations.

Fig. 10 shows the bed topography for Berkhoff et al.'s experiments. Initially, waves passing the shoal are refracted and wave energy converges behind the shoal. Due to diffraction a wave caustic forms as the rays cross. Berkhoff et al. measured wave heights along eight sections shown in Fig. 10, with experimental offshore wave conditions prescribed as: wave height $H_o = 0.0232$ m, wave period $T = 1.0$ s and incident wave angle $\theta_o = 0°$.

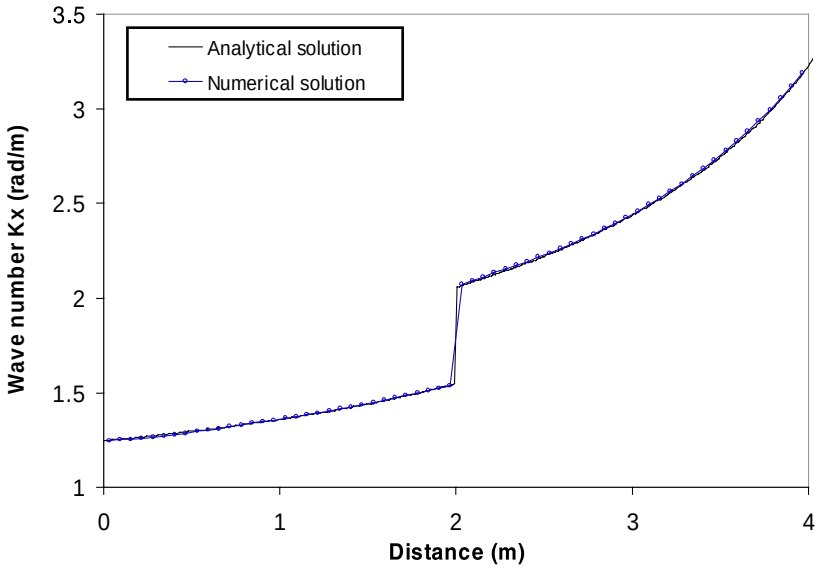

Fig. 8. One-dimensional wave flow over a step: wave number predictions including non-mild-slope solution.

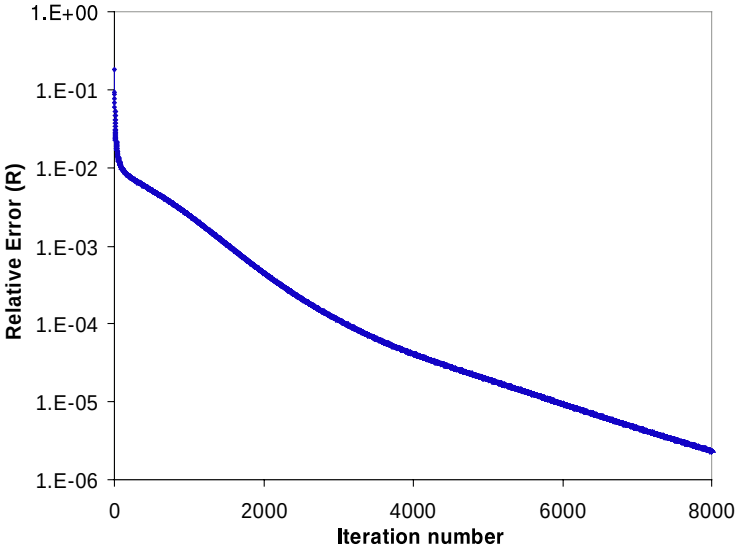

Fig. 9. One-dimensional wave flow over a step: convergence history.

In the classical ray-type approach, it is assumed that no energy is transferred across wave rays, so that in diffraction this fails to give a solution in caustic zones. The extra third-order diffraction terms (e.g., $\partial\delta^*/\partial x$) in Eqs. (5.2a)–(5.2c) are essentially a fix for the lateral transfer of energy along a wave crest, and should ideally be discretised using at least a third-order scheme. The present numerical scheme is a second-order

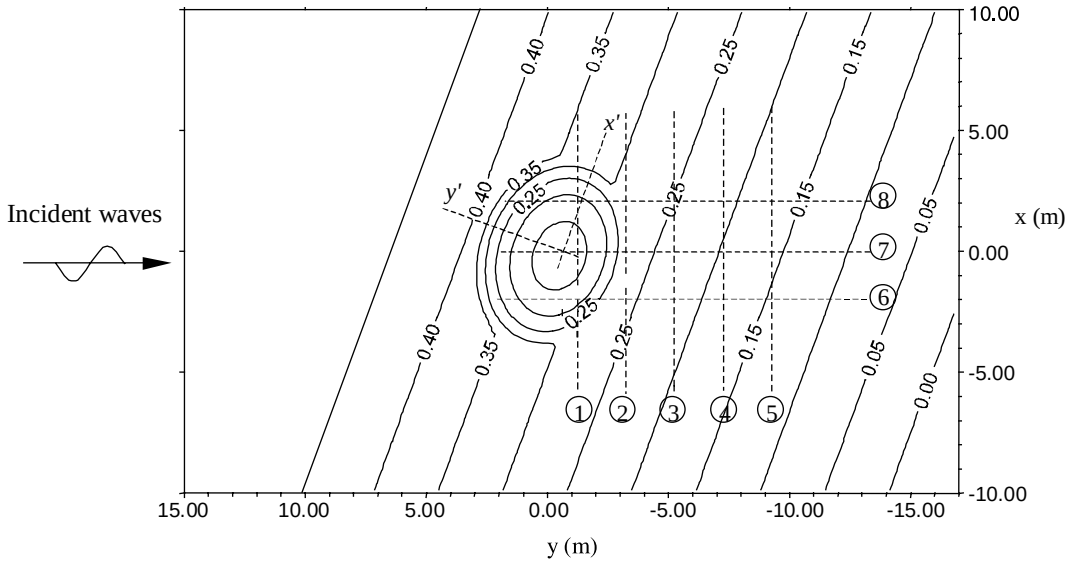

Fig. 10. Elliptical shoal: experimental and computational domain with bed contours (m) [5].

Godunov-type solver, but the requirement of a third-order discretisation can be relaxed in weakly-diffracted wave fields without having a significant detrimental effect on the solution, so that $\partial\delta^*/\partial x_i$ terms can be evaluated using finite differences. In our numerical simulations, a uniform grid was used where $\Delta x = \Delta y = 0.5$ m, the time step $\Delta t = 0.05$ s, the dimensionless eddy viscosity coefficient M_T was kept at 1.0, the minimum depth D_{min} set to 0.001 m with the roughness height being set to 0.001 m over the entire domain.

Fig. 11 shows wave vector plots at $t = 20$ s for cases without and with flux-gradient and source term balancing. In the latter case, the wave field at $t = 3$ s computed using the unbalanced formulation provides physically acceptable starting equilibrium values for the balanced scheme in order to accelerate the evolution of weakly and gradually varying waves. In the unbalanced case of Fig. 11(a), it can be seen that the wave vectors are unreasonably large at the shoreline and have evolved unphysically over the hump. The values of the wave numbers eventually render the scheme unstable. The balanced case in Fig. 11(b) shows no such unphysical behaviour with the direction of the wave vectors focussing wave energy behind the shoal. This is confirmed in Fig. 12(a), which shows the predicted relative wave height contours from the present scheme, where it can be seen that the balanced simulation has reproduced the wave focussing and attenuation in the lee of the shoal. The contours are similar to the experimental results given in Fig. 12(b) and alternative numerical results in the literature (e.g., [29,39]).

In Fig. 13, four representative plots of relative wave heights along different sections display the experimental data, the computed results of the present scheme, and for comparison, the results of Yoo and O'Connor [39] who solved the same equations but with a finite difference scheme. Ray-type models are averaged over one wave period and cannot account for all the rapid changes in wave phase responsible for the undulating wave height profiles in the experimental data. Such variations have to be modelled by more sophisticated nonlinear mathematical formulations that retain the correct phase information such as mild-slope models [26] or Boussinesq-type models [25]. However, the ray-type models offer a reasonable estimate with far less computational expense. When solving the wave conservation equations with a Godunov-type solver, it is clear from Fig. 11 that the wave heights displayed in Figs. 12 and 13 could not have been computed without balancing.

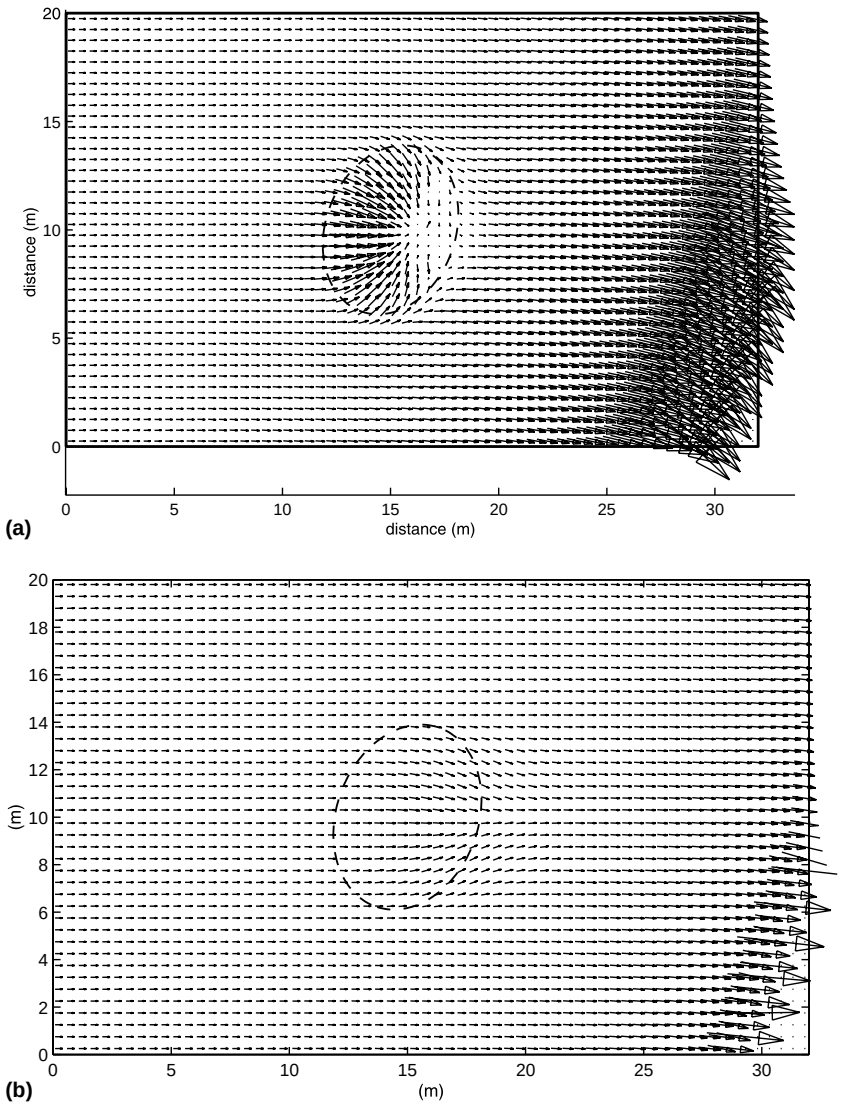

Fig. 11. Diffraction over an elliptical shoal: (a) Computed wave vectors at $t = 20$ s without balancing. (b) Computed wave vectors at $t = 20$ s with balancing.

5.3.3. Wave–current interaction at a sinusoidal beach

At real beaches currents are generated by variations in the bed topography and wave field. At rhythmic beach profiles, nearshore circulation cells (combinations of longshore currents and seaward directed rip-like currents) occur when the incident wave direction is almost normal to the beach. Laboratory studies have examined the flow patterns and current kinematics at half-sinusoidal beaches (e.g. [10,11]).

The experimental measurements of da Silva Lima [10] are used here for verification of the numerical scheme. Da Silva Lima's wave basin consisted of a half-sinusoidal plywood beach whose depth profile was specified by

$$h_s(x,y) = \begin{cases} sx, & -0.7\ \text{m} \leqslant x \leqslant 0, \\ s\left[x - 0.75 \sin\left(\frac{\pi x}{4.36}\right) \sin\left(\frac{2\pi y}{\lambda}\right)\right], & 0 \leqslant x \leqslant 4.36\ \text{m}, \end{cases} \tag{5.14}$$

where x is the distance offshore from the still water line (SWL), y is the distance alongshore ranging from 1.5 to 4.5 m, $s = 0.05$ is the slope of the plane beach and the so-called rip current spacing is $\lambda = 6$ m. Fig. 14 shows a definition sketch of the wave basin.

During the simulation, a time step of $\Delta t = 0.005$ s is utilised. The incident wave height is ramped up over a period of 20 s. The offshore wave conditions are: wave height $H_o = 0.0618$ m; wave period $T = 0.76$ s; and

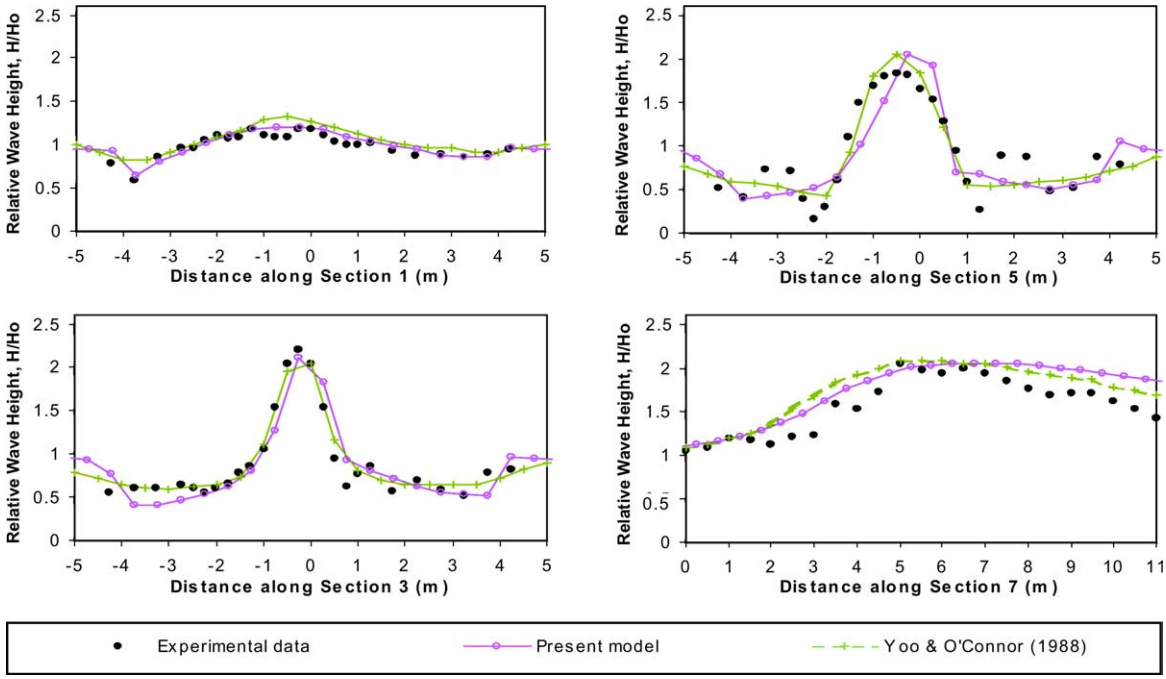

Fig. 13. Diffraction over an elliptical shoal: comparison of computed relative wave height along sections.

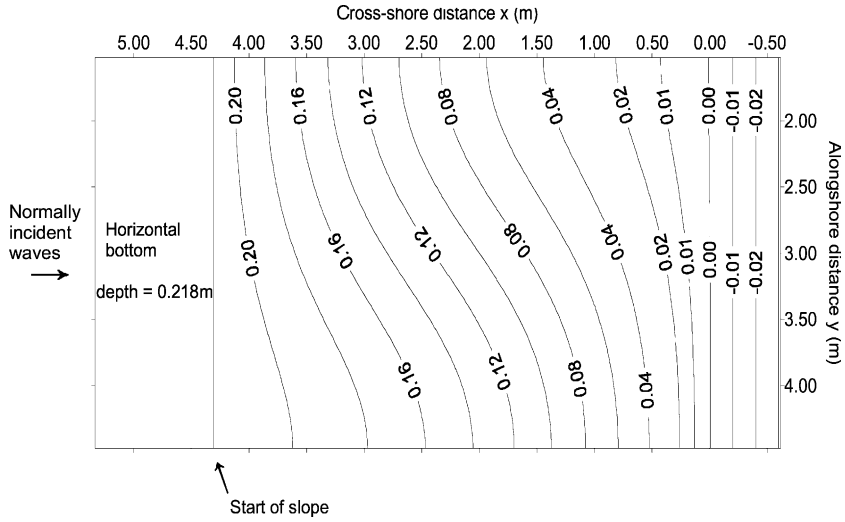

Fig. 14. Half sinusoidal beach: definition sketch.

incident wave angle $\theta_o = 0°$. A uniform 32×16 grid is used, where $\Delta x = \Delta y = 0.1875$ m. Wetting and drying at the shoreline is implemented according to Ebersole and Dalrymple's [13] scheme. For the case of a moving shoreline, careful consideration must be given to the definition of the equilibrium-state for a cell that is initially dry and becomes wet. When a cell is dry, there is no water so the equations are not active.

Therefore, with a given still water level, the equilibrium state in such cells is the dry condition ($u = v = 0$, $h = 0$). Hence, once an initially dry cell becomes flooded, the balanced equations are solved using the dry condition as the equilibrium state.

As mentioned in Section 5.3.1 for the case of wave flow over a step, the scheme is unstable in the absence of flux gradient and source term balancing. Wave vectors for unbalanced and balanced formulations are shown in Figs. 15(a) and (b) for the refracted wave fields over the half-sinusoidal beach. In this case, similar to Section 5.3.2, the wave field at $t = 1$ s computed using the unbalanced formulation provides physically acceptable starting equilibrium values for the balanced scheme. Once again it is clear that the splitting of the flux gradients and source terms in Eq. (5.11) must be balanced properly. The $S_h \partial\eta/\partial x_i$ terms are only

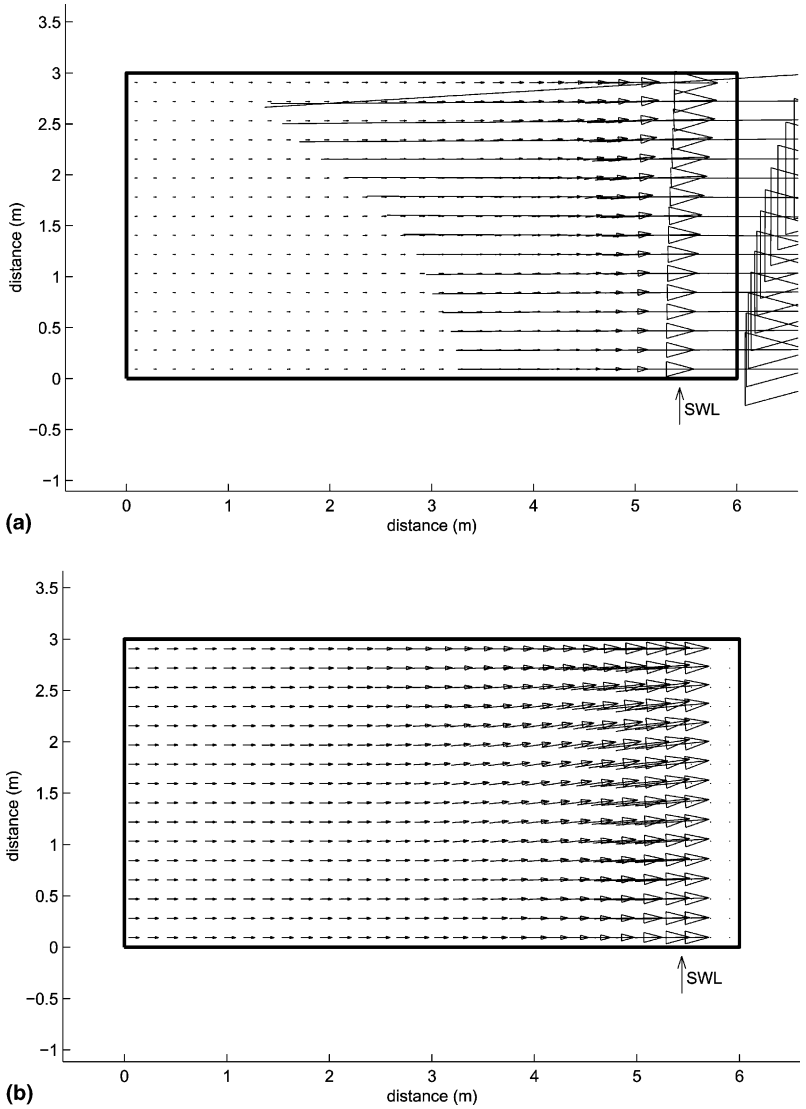

Fig. 15. Half sinusoidal beach: (a) Computed wave vectors at $t = 15$ s without balancing (*unstable*). (b) Computed wave vectors at $t = 15$ s with balancing.

weakly dependent on K_x and, when placed into the flux gradients, do not automatically balance the $S_h \partial h_s / \partial x_i$ terms in the source vector. This causes the values of K_x to grow. Unsurprisingly, such numerical instability is most acute at the shoreline and first manifests itself as unrealistically high wave numbers. Thus, appropriate balancing is required to give the physically correct wave field of Fig. 15(b).

Predicted depth-averaged currents are given in Fig. 16. A large primary gyre is located with its eye located about 1.74 m offshore of the still water line (SWL) in close agreement with the experimental result of da Silva Lima presented in Fig. 17 (where the rotational centre of the primary gyre is approximately 1.7 m

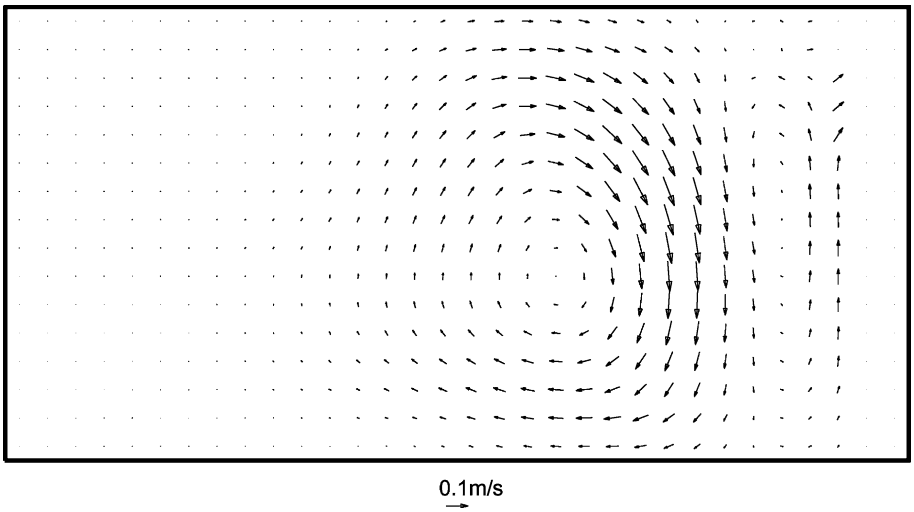

Fig. 16. Half-sinusoidal beach: depth-averaged velocities for level 5 grid.

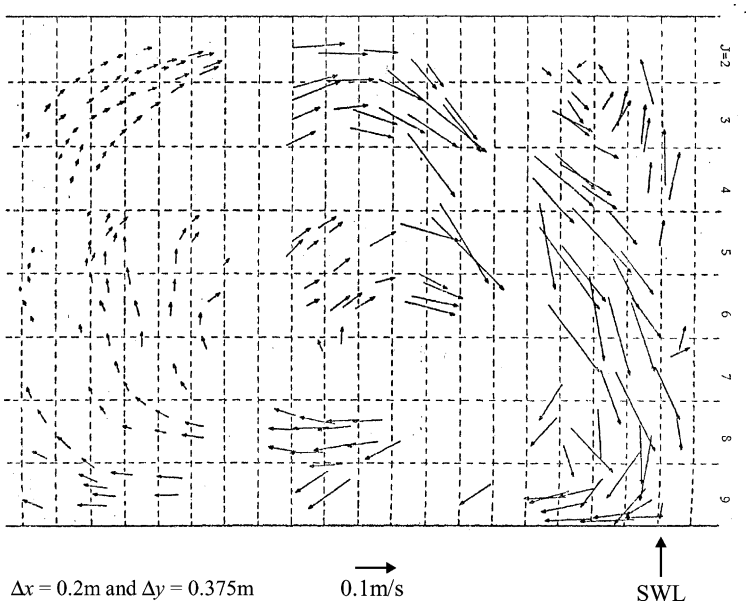

Fig. 17. Half-sinusoidal beach: experimental velocity vectors [10].

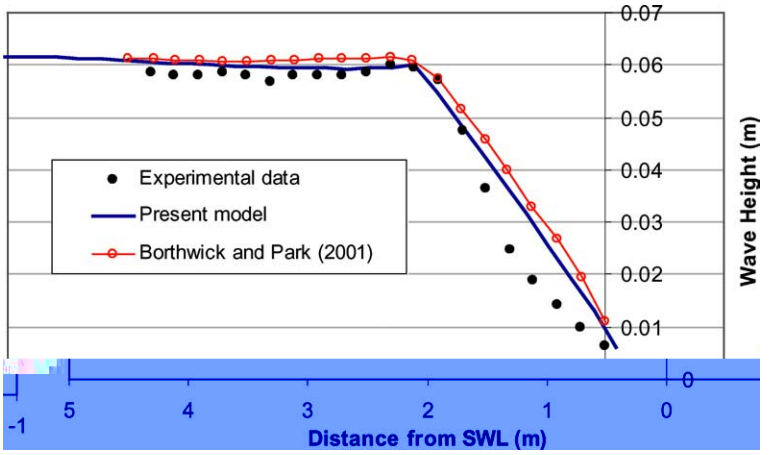

Fig. 18. Half-sinusoidal beach: experimental and computed wave heights along centreline of basin [10].

from the SWL). In contrast, Borthwick and Park [8], who used the same original mathematical formulation but with a first-order finite difference discretisation for the flux terms, produced a gyre of similar size, but located incorrectly at the centre of the basin. Also evident in the computational results, is the secondary gyre in the shallowest water depths.

The predicted wave heights along the cross-shore centreline of the basin displayed in Fig. 18 match Borthwick and Park's [8] numerical results and are in reasonable agreement with da Silva Lima's [10] experimental data. The results not only indicate that the wave-breaking criterion is well suited to this application, but also confirm the ability of the scheme to account correctly for the transfer of wave energy density.

6. Conclusions and further work

A new technique has been presented for mathematically conditioning hyperbolic matrix systems of conservation laws in finite volume Godunov-type schemes where Roe's approximate Riemann solver is used to model convective flux terms. While strictly still containing the root cause of the imbalance, extra physical information has been imposed so that the technique exploits the deviation from the equation system's unforced equilibrium as a means to bypass any possible numerical incompatibility between the flux-gradient and source terms. The technique has been applied to two different sets of equations to demonstrate its robustness. When applied to the shallow water equations, the technique works successfully for still water and wind-induced circulation in a dish-like circular basin. A demonstration case illustrated the unphysical results that are obtained for still water in a container with non-uniform bathymetry when the flux gradient and source terms in the shallow water equations are not balanced correctly a priori.

The balancing technique has also been applied to a Godunov-type solver of the hyperbolic period- and depth-averaged ray-type wave conservation and modified shallow water equations. Using an additional flux correction term, the model correctly simulates the converged wave number and wave height distributions over a stepped bed. Results are given for the diffracted wave field in the lee of a submerged shoal and of nearshore wave–current interaction at a semi-sinusoidal beach. When utilising Roe's Riemann solver for the convective wave fluxes, both cases demonstrate the importance of flux-gradient and source term balancing to obtain physically appropriate solutions in close agreement with laboratory data.

Inter-period coastal flow models are commonly based on Boussinesq-type equations [27], which contain additional terms (over and above the shallow water equations) consisting of third, fourth and fifth order mixed time and space derivatives. These terms are too complicated to be included in simple flux gradients and so have to be treated as source terms using conventional approaches, even when physically they are not source terms. Thus, further research is required on finite volume techniques that reflect the physical meaning of the high order terms in Boussinesq-type equations.

Acknowledgements

This work has been supported by the UK Engineering and Physical Sciences Research Council through EPSRC Grant GR/L29877 and co-investigated by Dr. K. Anastasiou and Dr. Z. Skoula of Imperial College, London. The authors are grateful for useful comments and suggestions provided by Professor Maria Elena Vázquez-Cendón of University de Santiago de Compostela, Spain, and Professor Guus Stelling of TU Delft.

References

[1] F. Alcrudo, P. García-Navarro, A high-resolution Godunov-type scheme in finite volumes for the 2D shallow-water equations, Int. J. Numer. Methods Fluids 16 (1993) 489–505.
[2] D. Ambrosi, Approximation of shallow water equations by Roe's approximate Riemann solver, Int. J. Numer. Methods Fluids 20 (1995) 157–168.
[3] K.A. Anastasiou, C.T. Chan, Solution of the 2D shallow water equations using the finite volume method on unstructured triangular meshes, Int. J. Numer. Methods Fluids 24 (1997) 1225–1245.
[4] J.A. Battjes, Refraction of water waves, J. Waterway, Port, Coastal Ocean Engrg., ASCE 94 (WW4) (1968) 437–451.
[5] J.C.W. Berkhoff, N. Booij, A.C. Radder, Verification of numerical wave propagation models for simple harmonic linear waves, Coastal Engrg. 6 (1982) 255–279.
[6] E.W. Bijker, The increase of bed shear in a current due to wave motion, in: Proceedings of the 10th International Conference on Coastal Engineering, ASCE, 1966, pp. 746–765.
[7] A.G.L. Borthwick, Q. Liang, B. Rogers, J.R. Ni, Dam-break simulations on uniform and Q-tree grids, in: Proceedings of the 8th International Symposium on River Erosion and Sedimentation, Cairo, November 3–5, 2001, on CD-ROM, 2001, pp. 1–10.
[8] A.G.L. Borthwick, K.-Y. Park, Quadtree grid numerical model of nearshore wave–current interaction, Coastal Engrg. 42 (2001) 219–239.
[9] J. Burguete, P. Garcia-Navarro, Efficient construction of high-resolution TVD conservative schemes for equations with source terms: application to shallow water flows, Int. J. Numer. Methods Fluids 37 (2001) 209–248.
[10] S. da Silva Lima, Wave-induced nearshore currents, Ph.D. Thesis, Liverpool University, UK, 1981.
[11] R.A. Dalrymple, R.A. Eubanks, W.A. Birkemeier, Wave-induced circulation in shallow basins, ASCE J. Waterway, Port, Coastal Ocean Div. 103 (WW1) (1977) 117–135.
[12] R.G. Dean, R.A. Dalrymple, Water Wave Mechanics for Engineers and Scientists, Prentice-Hall, New Jersey, 1984.
[13] B.A. Ebersole, R.A. Dalrymple, Numerical modeling of nearshore circulation, in: Proceedings of the 17th International Conference on Coastal Engineering, ASCE, vol. 4, 1980, pp. 2710–2725.
[14] M. Fujihara, A.G.L. Borthwick, Godunov-type solution of curvilinear shallow water equations, J. Hydraul. Engrg. 126 (11, November) (2000) 827–836.
[15] P. García-Navarro, M.E. Vázquez-Cendón, On numerical treatment of the source terms in the shallow water equations, Comput. Fluids 29 (2000) 951–979.
[16] L. Gascón, J.M. Coberán, Construction of second-order TVD schemes for nonhomogeneous hyperbolic conservation laws, J. Comput. Phys. 172 (2001) 261–297.
[17] S.K. Godunov, A difference method for the numerical computation of discontinuous solutions of hydrodynamic equations, Math. Sbornik 47 (89, 3) (1959) 271–306 (in Russian).
[18] N. Goutal, F. Maurel (Eds.), Proceedings of the 2nd Workshop on Dam-Break Wave Simulation, HE 43/97/016/B, Département Laboratoire National d'Hydraulique, Groupe Hydraulique Fluviale Electricité de France, France, 1997.
[19] A. Harten, J.M. Hyman, Self adjusting grid methods for one-dimensional hyperbolic conservation laws, J. Comput. Phys. 50 (1983) 235–269.

[20] H. Hirsch, Numerical Computation of Internal and External Flows, Computational Methods for Inviscid and Viscous Flows, vol. 2, John Wiley & Sons, New York, 1990.
[21] K. Hu, C.G. Mingham, D.M. Causon, Numerical simulation of wave overtopping of coastal structures using the non-linear shallow water equations, Coastal Engrg. 41 (2000) 433–465.
[22] M. Hubbard, P. Garcia-Navarro, Flux difference splitting and the balancing of source terms and flux gradients, J. Comput. Phys. 165 (2000) 89–125.
[23] C. Kranenburg, Wind-driven chaotic advection in a shallow model lake, J. Hydraulic Res. 30 (1) (1992) 29–46.
[24] R.J. LeVeque, Balancing source terms and flux gradients in high-resolution Godunov methods: the quasisteady wave-propagation algorithm, J. Comput. Phys. 146 (1998) 346–365.
[25] B. Li, C.A. Fleming, Three-dimensional method of Navier–Stokes equations for water waves, J. Waterway, Port, Coastal Ocean Engrg. 127 (1, Jan/Feb) (2001) 16–25.
[26] J.P.-Y. Maa, T.-W. Hsu, C.H. Tsai, W.J. Juang, Comparison on wave refraction and diffraction, J. Coastal Res. 16 (4) (2000) 1073–1082.
[27] P.A. Madsen, H. Bingham, Y. Agnon, The ultimate Boussinesq formulation for highly dispersive and highly nonlinear water waves, in: Proceedings of the 27th International Conference on Coastal Engrg, July 16–21, Sydney, Australia, Paper 35, 2000.
[28] M. Nugic, Efficient implementation of non-oscillatory schemes for the computation of free-surface flows, J. Hydraul. Res. 33 (1) (1995) 101–111.
[29] F.S.B.F. Oliveira, K. Anastasiou, An efficient computational model for water wave propagation in coastal regions, Coastal Engrg., ASCE (1998) 393–407.
[30] P.L. Roe, Approximate Riemann solvers, parameter vectors, and difference schemes, J. Comput. Phys. 43 (1981) 357–372.
[31] P.L. Roe, J. Pike, Efficient construction and utilisation of approximate Riemann solutions, in: Computing Methods in Applied Science and Engineering, North-Holland, Amsterdam, 1984.
[32] B.D. Rogers, A.G.L. Borthwick, P.H. Taylor, Godunov-type adaptive grid model of wave–current interaction at cuspate beaches, Int. J. Numer. Methods Fluids (2003), submitted.
[33] B. Rogers, M. Fujihara, A.G.L. Borthwick, Adaptive Q-tree Godunov-type scheme for shallow water equations, Int. J. Numer. Methods Fluids 35 (2001) 247–280.
[34] R. Soulsby, Dynamics of Marine Sands, Thomas Telford, UK, 1997.
[35] E.B. Thornton, Variation of longshore current across the surf zone, in: Proceedings of the 12th Conference on Coastal Engineering, ASCE, 1970, pp. 291–308.
[36] E.F. Toro, Shock-Capturing Methods for Free-Surface Shallow Flows, John Wiley & Sons, UK, 2001.
[37] US-CERC, Shore Protection Manual, US Army Coastal Engineering Research Center, US Corps of Engineers, Washington, DC, 1984.
[38] M.E. Vázquez-Cendón, Improved treatment of source terms in upwind schemes for the shallow water equations in channels with irregular geometry, J. Comput. Phys. 148 (1999) 497–526.
[39] D. Yoo, B.A. O'Connor, Diffraction of waves in caustics, J. Waterway, Port, Coastal Ocean Engrg. 114 (6) (1988) 715–731.
[40] D.H. Zhao, H.W. Shen, J.S. Lai, G.Q. Tabios III, Approximate Riemann solvers in FVM for2D hydraulic shock wave modeling, J. Hydraul. Engrg., ASCE 122 (12) (1996) 692–702.
[41] J.G. Zhou, D.M. Causon, C.G. Mingham, D.M. Ingram, The surface gradient method for the treatment of source terms in the shallow water equations, J. Comput. Phys. 168 (2001) 1–25.